Acta Biomaterialia 119 (2021) 390–404

Contents lists available at ScienceDirect

Acta Biomaterialia

journal homepage: www.elsevier.com/locate/actbio

Combining polarized Raman spectroscopy and micropillar compression to study microscale structure-property relationships in mineralized tissues

Tatiana Kochetkova[a,1,*], Cinzia Peruzzi[a,1], Oliver Braun[b,d], Jan Overbeck[b,d,e], Anjani K. Maurya[c,f], Antonia Neels[c], Michel Calame[b,d,e], Johann Michler[a], Philippe Zysset[h], Jakob Schwiedrzik[a,*]

[a] Empa, Swiss Federal Laboratories for Materials Science and Technology, Laboratory for Mechanics of Materials & Nanostructures, Thun, Switzerland
[b] Empa, Swiss Federal Laboratories for Materials Science and Technology, Transport at Nanoscale Interfaces Laboratory, Dübendorf, Switzerland
[c] Empa, Swiss Federal Laboratories for Materials Science and Technology, Center for X-Ray Analytics, Dübendorf, Switzerland
[d] Department of Physics, University of Basel, Switzerland
[e] Swiss Nanoscience Institute, University of Basel, Switzerland
[f] Cellular and Biomedical Sciences, Faculty of Medicine, University of Bern, Switzerland
[h] ARTORG Center for Biomedical Engineering Research, University of Bern, Switzerland

ARTICLE INFO

Article history:
Received 6 July 2020
Revised 7 October 2020
Accepted 22 October 2020
Available online 26 October 2020

Keywords:
Bone
collagen fibril orientation
quantitative polarized Raman spectroscopy
micropillar compression
failure mechanisms

ABSTRACT

Bone is a natural composite possessing outstanding mechanical properties combined with a lightweight design. The key feature contributing to this unusual combination of properties is the bone hierarchical organization ranging from the nano- to the macro-scale. Bone anisotropic mechanical properties from two orthogonal planes (along and perpendicular to the main bone axis) have already been widely studied. In this work, we demonstrate the dependence of the microscale compressive mechanical properties on the angle between loading direction and the mineralized collagen fibril orientation in the range between 0° and 82°. For this, we calibrated polarized Raman spectroscopy for quantitative collagen fibril orientation determination and validated the method using widely used techniques (small angle X-ray scattering, micro-computed tomography). We then performed compression tests on bovine cortical bone micropillars with known mineralized collagen fibril angles. A strong dependence of the compressive micromechanical properties of bone on the fibril orientation was found with a high degree of anisotropy for both the elastic modulus ($E_a/E_t = 3.80$) and the yield stress ($\sigma_a^y/\sigma_t^y = 2.54$). Moreover, the post-yield behavior was found to depend on the MCF orientation with a transition between softening to hardening behavior at approximately 50°. The combination of methods described in this work allows to reliably determine structure-property relationships of bone at the microscale, which may be used as a measure of bone quality.

Statement of significance

The structural complexity of bone contributes significantly to its mechanical properties across length scales. The bone lamella acts as the elementary building block, made up of aligned mineralized collagen fibrils embedded in an extrafibrillar matrix. This study aimed at establishing a method for

Abbreviations: MCF, mineralized collagen fibril; MTLT, mineralized turkey leg tendon; PRS, Polarized Raman spectroscopy; qPRS, quantitative Polarized Raman spectroscopy; FWHM, full width at half maximum; SNR, signal to noise ratio; EFM, extrafibrillar matrix; NCP, non-collagenous proteins; ROI, region of interest; SAXS, Small Angle X-ray Scattering; Micro-CT, Micro-computed tomography; FIB, focused ion beam; SEM, scanning electron microscope; STEM, scanning transmission electron microscopy; HR-SEM, high-resolution SEM; SEE, standard error of the estimate.

* Corresponding authors: Empa, Swiss Federal Laboratories for Materials Science and Technology, Laboratory for Mechanics of Materials & Nanostructures, Feuerwerkerstrasse 39, 3602 Thun, Switzerland. +41 58 765 63 08.
E-mail addresses: tatiana.kochetkova@empa.ch (T. Kochetkova), cinzia.peruzzi@empa.ch (C. Peruzzi), oliver.braun@empa.ch (O. Braun), jan.overbeck@empa.ch (J. Overbeck), anjani.maurya@empa.ch (A.K. Maurya), antonia.neels@empa.ch (A. Neels), michel.calame@empa.ch (M. Calame), johann.michler@empa.ch (J. Michler), philippe.zysset@artorg.unibe.ch (P. Zysset), jakob.schwiedrzik@empa.ch (J. Schwiedrzik).
[1] These authors contributed equally to this work.

https://doi.org/10.1016/j.actbio.2020.10.034

quantitative estimation of local fibril orientation and investigating its effect on the compressive micromechanical properties of isolated bone lamellae. Elastic modulus, yield strength, and post-yield characteristics were found to depend strongly on fibril orientation and could be well described by established composite models. The combination of methods described in this work can be used in future to assess bone quality by identifying tissue-scale structure-mechanical property relationships.

1. Introduction

Bone possesses outstanding mechanical properties as a result of its well-organized hierarchical structure and composition. However, metabolic bone diseases, like osteoporosis, drastically affect the bone structure and mechanical properties, leading to an increase in bone fragility. As the life expectancy of the population increases, so will the incidence of osteoporosis and fragility fractures [1,2]. Beyond quantity, bone fracture is predetermined by the bone quality, i.e. the combination of various parameters contributing to fracture resistance. At the moment, research groups all over the world are investigating various bone quality parameters that may lead to better bone fracture prediction [3,4]. Recently, attempts were made to correlate both bone composition and mechanical properties at different length scales with patient age, gender and bone metabolism state [5]. As there are numerous interdependent factors contributing to the bone quality, a promising approach for quantifying bone quality lies in the identification of tissue-scale structure-property relationships.

Hierarchical structure of bone. Bone is a composite biomaterial, made of mineral crystals (hydroxyapatite, 50-60 wt.%), proteins (mainly collagen type I, 30-40 wt.%) and water (bound and unbound, 10-20 wt.%) [6–8]. Each of these components contribute to the overall bone mechanical properties. Aligned mineralized collagen fibrils (MCF, ~30-300 nm in diameter) with intra- and extra-fibrillar hydroxyapatite crystals form sub-lamellar sheets (~1 µm thickness), a stack of which is called a lamella (~3-7 µm thickness). Further up the scale, lamellae form trabecular packets in cancellous bone, whereas in cortical bone concentric cylindrical layers of lamellae arranged around a central blood vessel form osteons (~200 µm in diameter). Lamellae may be considered as the main building blocks of bone and their mechanical properties are critical in defining overall bone mechanics [9].

Quantitative analysis of bone fibril orientation. Thanks to the recent progress in biomedical imaging, various modalities have been used for visualizing the spatial arrangement of MCF [10]. Some of the most frequently used techniques are polarized light microscopy [11], second harmonic generation microscopy [12,13], transmission electron microscopy [14] and small angle X-ray scattering (SAXS) [13,15]. However, those methods require complex sample preparation and do not provide additional information on the local chemical composition. Polarized Raman spectroscopy (PRS) is a powerful non-destructive imaging technique that has been long applied in compositional analysis in bone research. Raman spectroscopy allows to detect the frequency shifts of inelastically scattered light coming from the specimen exposed to a monochromatic light source, usually a laser. The resulting Raman bands are assigned to vibrations of characteristic chemical bonds, where for bone the bands of interest can be found in the range from 400-1800 cm^{-1}. Until now, polarized Raman spectroscopy has provided mostly qualitative information about spatial orientation of collagen fibrils in cortical bone [16–19]. In this work, we demonstrate that quantitative information can also be obtained in 3D, which we independently verify by SAXS, and then correlate with mechanical properties.

Mechanical properties of bone are strongly affected by the bone composition and structural anisotropy [20]. As an example, changes in the collagen network may lead to significant variations in the bone bending strength, elastic modulus, and work to fracture [21–23]. Recent studies show how bone elastic and post-yield mechanical properties are furthermore affected by variations in water content [24,25]. Bone mineral density (BMD) has been long employed in clinics for the indirect assessment of the mechanical behavior of bone and individual patient fracture risk estimations [26,27], however, it does not take into account the spatial distribution of bone material, structural anisotropy, or tissue properties. The hierarchical structure of bone leads to anisotropy of its mechanical properties. Bone fracture is a multiscale process and needs to be studied at all relevant scales. The dependence of macroscale mechanical properties of cortical bone on the loading direction has been investigated for half a century and is mainly related to the osteonal orientation [28]. Later, the anisotropic mechanical properties of single osteons were identified [29,30], demonstrating the importance of lamellar organization in governing the osteonal mechanical response. Over the past four decades, the directional dependence of mechanical properties has been studied more extensively at the length scale of a bone lamella [31–34], which is significantly affected by the underlying MCF orientation. Although lamellae may be considered as the main building block of bone, to the best of our knowledge, no reports have been published describing the influence of mineralized collagen fibril orientation in a continuous range between 0°- 90° on their elastic, yield, and post-yield mechanical properties. Filling this knowledge gap would allow determining the structure-property relationships of bone at the lamellar length scale, which is a prerequisite for the development and validation of reliable multiscale models predicting bone failure.

Micromechanical testing on bone is an attractive technique to study bone mechanical properties, as it allows to limit the influence of local structural and compositional inhomogeneities on the overall mechanical response. The field of micromechanical testing of bone is rapidly progressing: starting from the pioneering works on bone nanoindentation [35,36] and going towards the state-of-the-art microscale tensile [34,37], compression [32,38–40] and bending [9] experiments on the lamellar or even the mineralized collagen fibril level [15,41]. One of the most common micromechanical testing techniques for bone is indentation [42], however its interpretation in terms of post-yield behavior is complex [43]. Micropillar compression is a novel experimental method [44], where cylindrical samples with dimensions in the micrometer range are prepared by focused ion beam and subsequently compressed using a flat punch indenter. Unlike in classical indentation, the loading in the specimen is mostly uniaxial, which simplifies the interpretation of the output load-displacement curves in terms of stress-strain behavior. In this study, we performed micropillar compression experiments of cortical bone lamella under humid conditions, with a known collagen fibril orientation.

The aims of this study were to (i) establish a quantitative method for MCF spatial orientation estimation based on PRS and (ii) investigate the effect of MCF orientation on the yield stress and elastic modulus of cortical bone lamellae. For the first part, polarized Raman measurements were carried out on mineralized turkey leg tendon, a model material with known fibril spatial orientation [45], and then validated on bovine cortical bone osteonal lamellae. For the mechanical study, micropillar compression experiments were performed on isolated bovine cortical bone lamellae with MCF orientations ranging from 0° to 82° with respect to the loading direction.

2. Materials and methods

2.1. Samples

As a model material for polarized Raman calibration, **mineralized turkey leg tendon (MTLT)** was used. The main advantage of MTLT tissue is its simplified fiber arrangement compared to mammalian cortical bone structure. MTLT is composed of densely packed collagen fibrils, strongly aligned with the tendon axis [45–47], which means that global and local fibril orientation are highly correlated.

MTLT samples were prepared from a turkey leg, obtained from a local abattoir. Highly mineralized parts were dissected from the tendon bundles, mechanically cleaned and further cut with a diamond band saw under constant water irrigation (Exakt, Norderstedt, Reichert-Jung, Germany). The resulting tendon pieces of about 1.5 mm in diameter and 4.0 mm in length were dried under ambient conditions for 24 h. For the PRS calibration, MTLT pieces were fixed on specially designed aluminum SEM stubs with a 2-component epoxy resin adhesive (Schnellfest, UHU, Germany) and cut at a specific angle to the main tendon axis using a high-precision diamond band saw (Leica EM TXP, Germany). Finally, the exposed specimen surfaces were polished with progressive grades of silicon carbide paper and finished manually on a soft cloth with a 1 µm diamond suspension followed by 0.04 µm SiO_2 suspension resulting in a polished sample surface virtually parallel to the stub surface. A total of five specimens were prepared, each containing a tendon section cut at 0°, 22.5°, 45°, 67.5° or 90° to the main tendon axis (Figure S1, Supplementary information A). The samples cut at 0° and 90° are referred to as axial and transverse samples, respectively. For precise MCF angle determination, small angle X-ray scattering measurements were performed on each sample (Section 2.3).

Combined PRS and micropillar compression measurements were performed on **bovine cortical bone**, which represents an intermediate model material between the MTLT and human cortical bone. Bovine cortical bone, in comparison to human, exhibits higher mineralization, yielding a higher strength [48], however, zones with a similar microstructural organization with distinguishable osteonal and interstitial zones can be found in both tissues [49]. It should be noted that the lamellar arrangement in bovine cortical bone primary osteons has a more uniaxial orientation (as demonstrated in Supplementary information B.3) in comparison to more complex MCF orientation patterns observed in human osteonal lamellae [50]. This makes bovine cortical bone an attractive animal model for basic research, prior to translation to human bones.

A bovine tibia was obtained from a local abattoir. Three medial slices of cortical bone from the diaphysis were cut radially into smaller sections. Posterior quadrant sections with higher osteonal bone content were used for further processing steps (Figure S2, Supplementary information A). The bone samples (~5 mm cubes) were glued to specially designed SEM stubs and cut at five angles between 0° and 90° with respect to the longitudinal bone axis, following the same protocol as the MTLT specimens. In order to obtain plane surface for compression experiments, samples were additionally ultra-milled (Polycut E, Reichert-Jung, Germany) and consequently polished with 1000 grid silicon carbide and paper cloth with 0.3 µm Al_2O_3 lubricant. For micropillar fabrication after PRS measurements, the bovine cortical bone samples were additionally sputtered with 11 nm thick Au film (Leica EM ACE600, Germany) and a thin film of silver paste (Plano GmbH, Germany) was applied at the sample sides down to the aluminium holder to minimize the drift caused by electrostatic charging under the electron or ion beams. Considering the dimensions of the mechanically tested bone volumes (5 µm in diameter), the effect of the thin Au film (11 nm thickness) on the measured mechanical properties can be neglected. In total, 26 primary osteons with different orientations from 0° to 90° were chosen from 5 bovine cortical bone samples for the PRS measurements, 13 of which were then used for micropillar compression measurements.

2.2. Raman spectroscopy and data processing

In the present work, we used polarized Raman spectroscopy for quantitative orientation estimation of MCF in mineralized tissues. For this, the polarized Raman spectral response of MCF was theoretically and experimentally correlated with the fibril orientations.

Raman spectra were acquired using a WITec Alpha 300 R confocal Raman microscope in backscattering geometry. A diode-pumped linearly polarized continuous 785 nm laser was used in combination with a 50 × objective (0.80 numerical aperture). The linear polarization of the exciting laser was adjusted with a motorized λ/2 plate. No analyzer plate was included in the light path after the sample. The Rayleigh scattered light was blocked by an edge filter. The backscattered light was coupled to a 400 mm lens-based spectrometer with a grating of 300 g/mm equipped with a cooled deep-depletion CCD. The laser power was set to 30 mW, the estimated full width at half maximum (FWHM) of the focal spot was ~0.4 µm in lateral and ~1.7 µm in axial direction, as calculated from the confocal Rayleigh criteria [51]. At each region of interest (ROI), Raman spectra were collected at different excitation polarizations from 0° to 180° with a 10° polarization angle step and 30 s integration time. As a result, a set of 19 polarized Raman spectra was collected for a single ROI. For each MTLT sample, PRS measurements were carried on 5 to 8 ROI, whereas for bovine cortical bone sample a single ROI was measured per osteon. In total, 33 ROI were measured for the MTLT samples, corresponding to 5 different out-of-plane orientation, and 26 ROI for bovine samples, corresponding to 26 osteons with different out-of-plane orientation. Spectral analysis was done in a batch mode using Python v3.6 [52] and consisted of background removal, location of the peaks of interest (amide I, amide III, ν_1PO_4, ν_2PO_4, CH bending) with consequent double or triple Lorentzian peak fit using a least square scheme (scipy.optimize.leastsq). The detailed PRS analysis procedure is described in Supplementary information B.1, output spectra for different laser polarization angles are presented in Figure 1.

The intensity of the Raman scattering depends on the molecular bond orientation relative to the laser polarization vector, as well as the excited vibration mode. As shown previously [16–19], by collecting Raman spectra at different orientations of the incident polarized laser light, the anisotropic spectral response of the amide I band (mainly C=O stretching) can be used to derive information about the orientation of the collagen molecules [17,53–55]. At the same time, the amide III band is considered as polarization-insensitive, as this vibration mode mainly involves N-H bending and C-N stretching that are equally distributed across the collagen amino acid sequence, which results in homogeneous Raman scattering [53,56–58]. In this study, the MCF spatial orientation was estimated from the integrated area ratio of the amide I over the amide III band collected at different laser polarizations.

The theoretical calculations of amide I over amide III ratios at different laser polarization are in good agreement with the experimental data for 0° and 90° out of plane fibril angle as shown in Figure 1 and Supplementary information B.1. For the quantitative measurement of polarization anisotropy of a given set of polarized experiments in a single ROI, we used the simplified description proposed by Bao et al. [59]:

$$f(\alpha,\ \varphi) = A\cos^2(\alpha+\varphi) + B\sin^2(\alpha+\varphi). \quad (1)$$

Where α is the polarization angle of the laser, $\frac{A}{B}$ the introduced parameter of anisotropy ($\frac{A}{B} \to 1$ for isotropic sample), and φ the

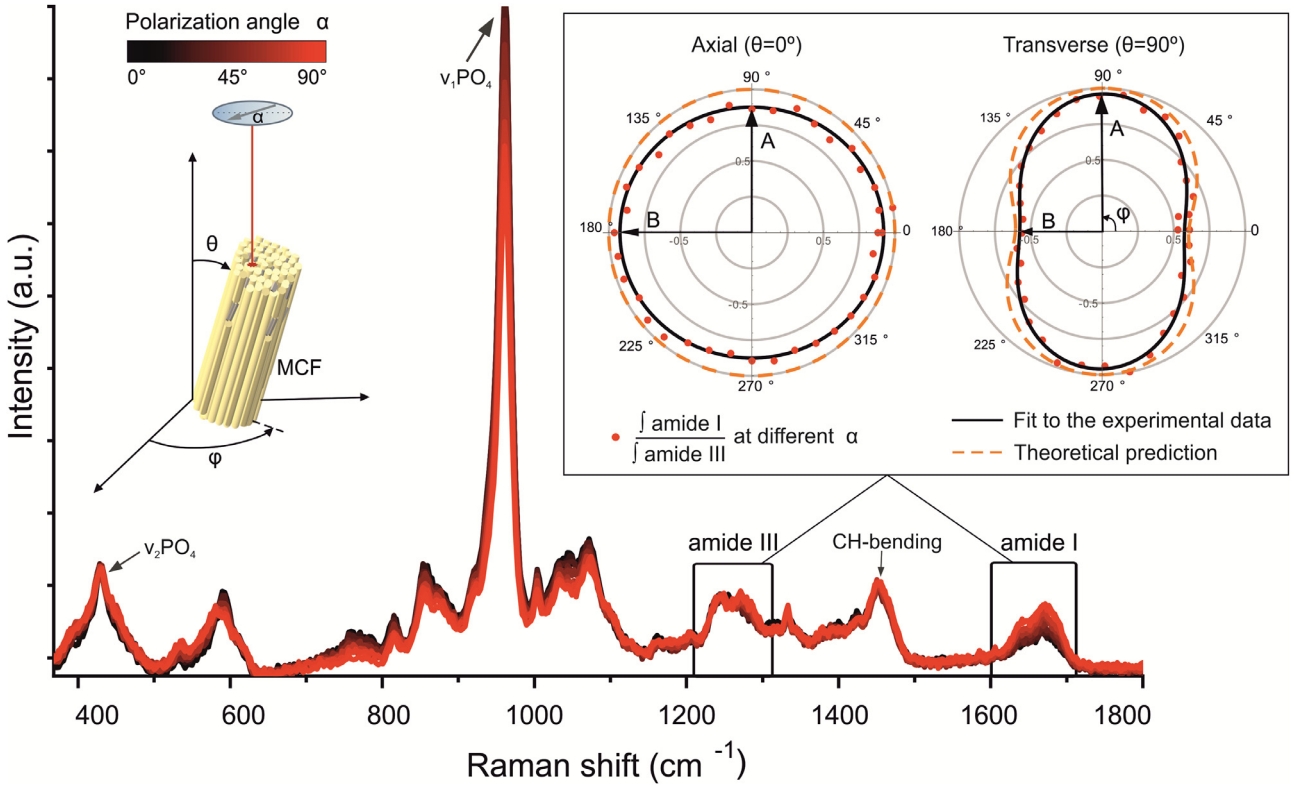

Figure 1. MCF spatial orientation during Raman spectra acquisition with marked out-of-plane (θ) and in-plane (φ) angles. Set of Raman spectra collected at different incident laser polarization on MTLT. Highlighted characteristic collagen bands: amide III (1215–1300 cm^{-1}, N–H bending and C–N stretching of the peptide backbone) and amide I (1600–1700 cm^{-1}, C=O stretching). Polar plots: polarization dependence of ∫amide I / ∫amide III with theoretical prediction and simplified fit to the experimental data (1) for two assumed orthogonal MCF orientations.

in-plane rotation angle for fibrils with respect to the laser polarization. The parameter of anisotropy A/B depends on the out-of-plane fibril orientation, the exact relationship was determined by calibration on the MTLT samples. The Raman spectra with highlighted amide peaks and output polar plots with theoretical predictions and fit to the experimental data (1) for axial (parallel to the incident laser beam) and transverse (orthogonal to the incident laser beam) collagen fibrils orientation are shown in Figure 1.

To assess the variation in bone mineralization, the ratio of the secondary phosphate (v_2PO_4, 370-500 cm^{-1}) over the amide III integrated intensity was analyzed. Following the study of Roschger et al. [60], the mineral to matrix ratios (v_2PO_4/amide III), can be correlated to the Ca content. For each ROI, the mineral to matrix ratio was averaged over 19 spectra. The mineral crystallinity [53,61–63] was assessed from 1/FWHM of the primary phosphate (v_1PO_4, 920-1000 cm^{-1}) and averaged over all laser polarizations for each ROI. To assess the variation of the non-collagenous proteins (NCP) content, the C-H bending at 1360-1500 cm^{-1} was analyzed, to which both collagen and NCPs contribute [64]. Since amide III is polarization-independent and almost exclusively representative of the collagen phase, following the reasoning of Katsamenis et al. [65], the Raman integrated intensity ratio of amide III / CH bending was used to quantify the relative concentrations of collagen versus NCPs.

2.3. Independent verification of MCF orientation

Small Angle X-ray Scattering (SAXS) experiments were performed on MTLT samples to validate fibril alignment after sample fabrication. SAXS experiments were performed with a Bruker Nanostar instrument (Bruker AXS GmbH, Karlsruhe, Germany). The instrument was equipped with a pinhole collimation system, a micro-focused X-ray Cu source (wavelength Cu Kα = 1.5406 Å) and a 2D MikroGap technology-based detector (VÅNTEC-2000 with 2048 × 2048 pixels and 68 × 68 μm each pixel size) along with a custom built semi-transparent beam stop. The beam size at sample position was about 400 μm in diameter. The instrument provided a resolvable scattering vector modulus q in a range between 0.06 - 2.1 nm^{-1} for a 107 cm sample to detector distance. The scattering frames were recorded for 1800 s at room temperature in moderate vacuum condition of about 10^{-2} mbar to reduce air scattering. Prior to the experiments, the sample to detector distance was calibrated with standard silver behenate powder samples.

The misorientation width and true orientation of MCF with respect to the sample and holder surface in the MTLT samples was estimated from the streak-like diffuse scattering in 2D SAXS profiles. This streak is produced by extended scattering objects (i.e. collagen fibrils) along the fiber axis of the fibrous materials [66,67]. The true orientation of collagen fibrils was determined by averaging the center values obtained from fitting the extracted azimuthal scans (q-range of 0.356 - 0.783 nm^{-1} with step size of 0.036 nm^{-1}) with a Lorentzian function (see Supplementary information D.1). The collagen fibrils misorientation width was calculated using the Ruland streak method [68,69]. In this method, the azimuthal broadening of intensities along the streak axis is evaluated and linked to the fibril misorientation (Supplementary information D.2).

Micro-computed tomography (micro-CT) scans of the bovine bone specimens (µCT 100, SCANCO Medical AG, Switzerland) were collected on each of the bovine bone samples to access osteon orientation after sample preparation. Samples were scanned at a spatial resolution of 4.9 µm with 45 kVp energy, 200 μA tube current and 2 × 400 ms integration time. The spatial orientation of the osteons was estimated using ImageJ 1.52v [70] and BoneJ 1.4.3 [71] as

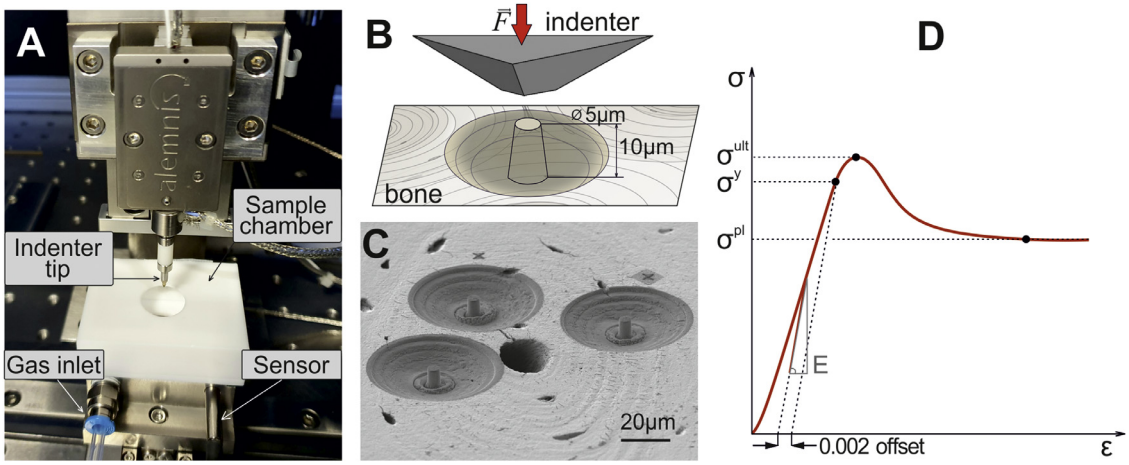

Figure 2. Schematic of micropillar compression test. (A) Indenter setup with controlled humidity sample chamber. (B) Sketch of the micropillar compression configuration. (C) HRSEM image of fabricated micropillars. (D) Stress-strain curve with marked output parameters: elastic modulus $\boldsymbol{E}$, calculated as the slope of the stress-strain curve during the partial unloading segment; yield stress $\boldsymbol{\sigma^y}$, defined as stress at 0.2% inelastic deformation; ultimate stress $\boldsymbol{\sigma^{ult}}$ is the maximum stress value; plateau stress $\boldsymbol{\sigma^{pl}}$ is the stress value at 0.08 strain.

a screening step to choose osteons for later qPRS analysis. Firstly, the global sample tilt of each sample scan was corrected using the Untilt Stack plugin. Secondly, the osteons of interest were located and isolated by combining optical microscopy with micro-CT images. Output stacks were binarized using Otsu's threshold clustering algorithm. Prior to calculations, Haversian canals were checked for irregularities: only the top segments without branching or sudden changes in orientation were used. Using the Moment of Inertia plugin, three orthogonal principal axes were automatically determined for each Haversian canal and the rotation matrix in reference to the stacks main axis was constructed. The out-of-plane orientation of each osteon was taken as the angle between the principal axis along the Haversian canal and the z axis of stacks. The angle was extracted from the rotation matrix and correlated later with the polarized Raman measurements. For more details see Supplementary information E.

2.4. Mechanical testing and analysis

Bone micropillars were fabricated using a focused ion beam workstation (Tescan Lyra, Czech Republic) with a well-established three step protocol described elsewhere [32,38]. Within each bovine bone sample, 5 osteons were selected for compression tests. Depending on the osteonal morphology, 2 to 3 pillars were fabricated. Each pillar had a diameter of approximately 5 µm and an aspect ratio of 2, as determined from HRSEM imaging (Hitachi S-4800, Japan). Examples of fabricated micropillars are shown in Figure 2 C.

A self-developed *ex situ* indenter setup was used in this study. The system is based on commercial hardware for actuation, sensing, and electronics (Alemnis AG, Switzerland). The experiments were conducted in displacement control to keep the strain rate constant even after the yield point. The system included an optical microscope to visualize the sample surface and to locate micropillars for compression tests and a custom environmental chamber. The relative humidity was controlled using a continuous gas stream from a humidity generator (WETSYS, Setaram, France) and feedback from a relative humidity sensor inside the chamber. The overview of the indenter setup and the schematic of the experiment are shown in Figure 2.

Compression experiments were performed at ambient temperature and pressure, the relative humidity was set to 93 % for at least 4 h prior to the compression experiments, ensuring hydration equilibrium of the sample. Pillars were compressed with a flat punch indenter tip with a diameter of 20 µm. The micropillar compression was performed in displacement control up to a maximum depth of 1 µm (10 nm/s loading rate) corresponding to a strain rate of $10^{-3}\ s^{-1}$ with an intermittent unloading segment in the elastic region, which was used for the calculation of the elastic moduli (Figure 2 D).

As micropillar compression features uniaxial loading, the stress-strain data was assessed from the load-displacement curves after frame compliance and pillar sink-in corrections [72]. The elastic modulus values were extracted from the loading/unloading cycle in the elastic region and the yield stress was computed as the stress that is needed for a plastic deformation of 0.2%. These properties were determined for every pillar using a custom Matlab code (R2018a, MathWorks Inc., Natick, MA, USA). After compression, the micropillars were imaged with a HRSEM.

2.5. Mechanical modeling

Apparent elastic modulus E_{app} was modeled as a function of collagen fibril orientation (Supplementary information F.1):

$$E_{app} = \left(\frac{\mathrm{Cos}^4(\theta)}{E_a} + \frac{\mathrm{Sin}^4(\theta)}{E_t} + \left(\frac{1}{\mu_a} - 2\frac{\nu_a}{E_a} \right) \mathrm{Cos}^2(\theta)\mathrm{Sin}^2(\theta) \right)^{-1}. \quad (2)$$

Elastic moduli were extracted from micropillar compression tests and fibril orientation from PRS measurements, where E_a and E_t are the axial and transverse elastic modulus values accordingly, ν_a and ν_t the Poisson ratios and μ_a the shear modulus.

Yield stress was modeled as a function of collagen fibril orientation using the Tsai-Hill composite failure criterion (Supplementary information F.1) [73]. For unidirectional fiber-reinforced composite materials subjected to in-plane stress, the failure criterion is given by:

$$\sigma_x = \left(\left(\frac{cos^2(\theta)}{X} \right)^2 - \left(\frac{sin(\theta)cos(\theta)}{X} \right)^2 + \left(\frac{sin^2(\theta)}{Y} \right)^2 + \left(\frac{sin(\theta)cos(\theta)}{S} \right)^2 \right)^{-1/2}, \quad (3)$$

where σ_x is the stress applied along the loading axis; X, Y and S symbolize the longitudinal, transversal and shear strength of

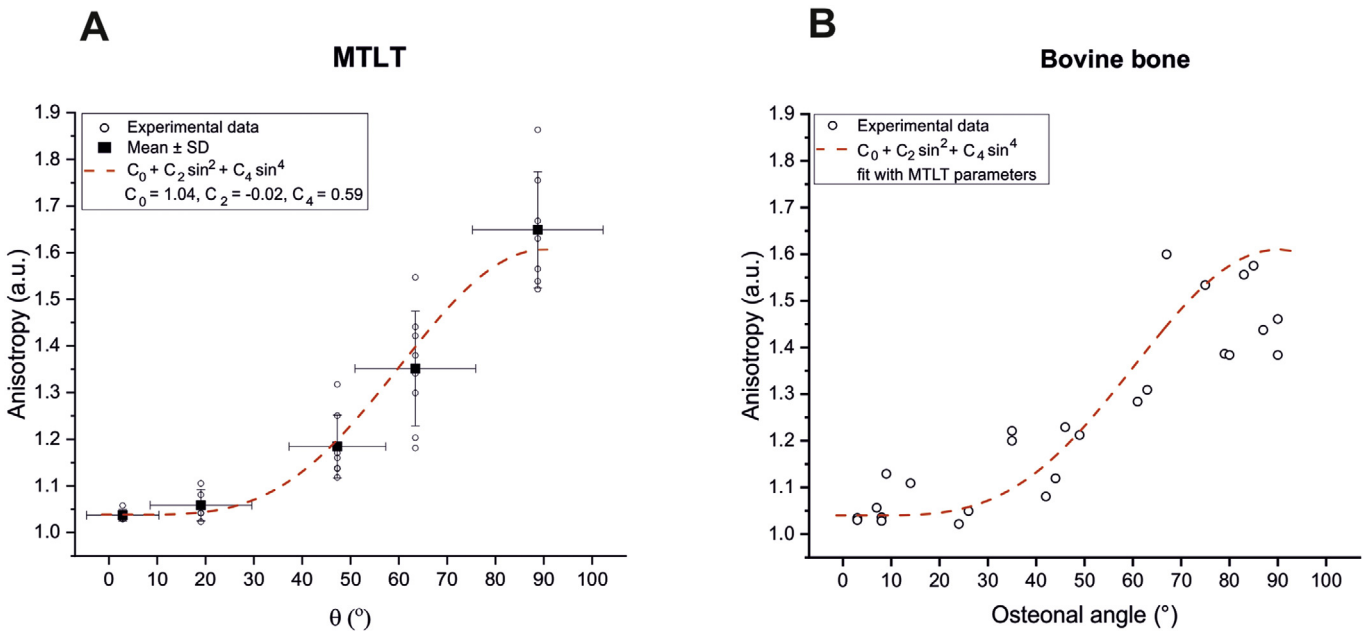

Figure 3. (A) Anisotropy of MTLT collagen bands at different out-of-plane fibril orientation $\boldsymbol{\theta}$; (B) Anisotropy of bovine cortical osteonal bone collagen bands at different osteon orientation, fitted with the calibration function from the MTLT study. The coefficients of determination R^2 are 0.98 and 0.82, respectively.

the composite. Here, bovine cortical bone yield strength was expressed as a function of MCF angle by fitting Eq. (3) with individual strengths obtained from micropillar compression tests and fibril orientation assessed from PRS.

2.6. Statistical data analysis

All data manipulations were performed using Python v3.6 [52] and MATLAB R2019b [74]. Measurements are reported as mean ± standard deviation. All non-linear curve fittings reported in this study were done using least squares regression (scipy.optimize, Python v3.6). The goodness of the non-linear fit was estimated from the coefficient of determination R^2 (sklearn.metrics) at $p < 0.05$, $R^2 = 1$ being the best possible score. Multiple linear regression analysis was performed using Python (sklearn.linear_model, statsmodels), the criterion for significance was $p < 0.05$.

3. Results

3.1. qPRS calibration on MTLT and validation study on bovine cortical bone lamella

Polarized Raman spectra were collected from the MTLT samples with known out-of-plane MCF angles θ measured by SAXS. For each MCF orientation 19 PRS measurements were taken on 5 to 8 ROI. The anisotropy parameter A/B, describing the maximum variation of the amide I/ amide III integral area as a function of incident laser polarization, was calculated for each of the samples by fitting equation (1). The anisotropy parameter A/B was then correlated with the fibril out-of-plane angle θ, taken from the SAXS measurements (Figure 3A).

SAXS measurements were used for structural analysis of MCF in tendon samples cut at five angles between 0° and 90°. To correlate the average MCF orientation in the sample measured by SAXS with the local MCF orientation measured by PRS, the SAXS measurements report the mean MCF out-of-plane angles θ together with the misorientation width of MCF determined by the Ruland method. From the azimuthal broadening of SAXS scattering intensities along the streak axis, the mean MCF out-of-plane angles θ were found to be close to the initial sample cutting angles: 2.88°±0.06°, 19.06°±0.05°, 47.28°±0.08°, 63.43°±0.06° and 88.76°±0.04°. Following the Ruland streak method, the misorientation width of MCF was found to be higher for the higher out-of-plane angles θ, ranging from 15° to 27° (for more details see Supplementary information D.2).

Theoretical calculations were used to determine the functional dependence of the anisotropy parameter A/B on the MCF out-of-plane orientation, see supplementary information B.2 for further details. We found that a function of the form (4) is well suited to reproduce the theoretical prediction and retains the 180° periodicity (R^2=0.99, Supplementary information B.2).

$$f(\theta) = C_0 + C_2 sin^2(\theta) + C_4 sin^4(\theta), \quad (4)$$

The average anisotropy parameter A/B from the PRS measurements on each of the MTLT specimens was fitted with Eq. (4) versus the fibril out-of-plane angle (coefficient of determination R^2=0.98). The out-of-plane angular error in Figure 3 A represents the fibril misorientation width, as determined from the SAXS measurements. From the MTLT fit, the following parameters of the calibration function (4) were found: $C_0 = 1.04$, $C_2 = -0.02$ and $C_4 = 0.59$. The qPRS out-of-plane angles were compared to the SAXS out-of-plane MCF angles and the standard error of the estimate (SEE) was taken as the angular uncertainty resulting in an error estimate of $\theta^{err} = 9.7^\circ$ (Supplementary information B.5).

Next, polarized Raman spectra were collected on 26 bovine cortical bone osteons with different orientations from 0° to 90°, as measured by micro-CT. Figure 3 B shows a correlation between the anisotropy parameter A/B for bovine cortical bone and the out-of-plane angles of the osteons. The data was compared to Eq. (4) with the parameters determined from the MTLT calibration and the osteon angles taken for θ (coefficient of determination R^2=0.82).

The out-of-plane MCF angles θ are extracted numerically from function (4). By extracting both the out-of-plane angle θ (Eq. (4)) and the in-plane angle φ (Eq. (1)) from the PRS spectra, a quantitative 3D orientation estimation of the MCF is possible. For further mechanical parameter analysis, we focused on the out-of-plane MCF angles θ.

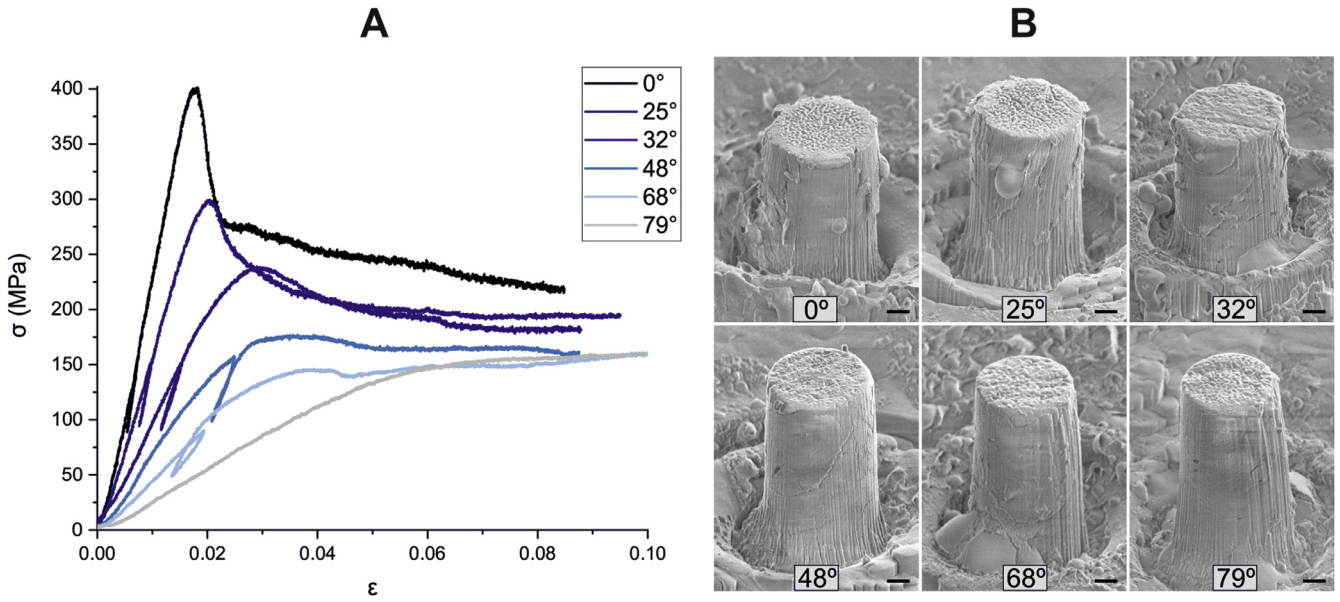

Figure 4. Stress-strain curves and HRSEM images after pillar compression of bovine cortical bone lamella with different mineralized collagen fibril orientation, scale bar 1 µm.

3.2. Micropillar compression of bovine cortical bone lamella with known fibril orientation

Microscale compression tests were performed on FIB manufactured micropillars with known collagen fibril orientation measured by qPRS. A total of 44 micropillars were fabricated in 13 osteons on the bovine cortical bone samples, from which two had irregularities in geometry and were therefore excluded from the study, three were lost due to operator errors and three were excluded from the batch analysis due to excessive noise in the force-displacement data. The remaining micropillars (N=36) were used for the actual testing and analysis. As a result, 2 to 3 micropillars were tested for each collagen fibril orientation (N=13). Representative stress-strain curves as a function of the fibril angle, determined by qPRS, and the images of corresponding micropillars after compression are shown in Figure 4.

The collected stress-strain curves for different MCF orientations (Figure 4 A) demonstrate a clear dependency of the mechanical response on the fibril angle. This dependence is even more pronounced in Figure 5, where elastic moduli and yield stress, extracted from the stress-strain curve, are plotted versus the out-of-plane MCF angles, known from previously performed qPRS measurements. The elastic modulus of lamellae with collagen fibrils parallel to the loading direction is more than 3.8 times higher than the modulus of lamellae with fibrils orthogonal to the loading direction. Similar behavior was observed for the yield stress, where axially aligned samples show a yield stress almost 2.5 higher than transverse samples. For further fitting, the mean values of the elastic moduli for each of the fibril orientation were used. The apparent elastic moduli were fitted as a function of MCF angles with the analytical expression for the apparent modulus in axial direction of a transversely isotropic compliance tensor rotated around one axis from the transverse plane (Eq. (2)). For the analysis, the axial elastic modulus E_a was taken as the maximum value found from the micropillar compression tests and the transverse elastic modulus E_t was calculated as the average measured modulus of compression experiments of micropillars with a fibril angle $> 60°$. The remaining free parameters ν_t, μ_a were determined using a least-squares fit of the fibril angle dependent data. The mean values of the yield stress for each of the fibril orientation were fitted with the Tsai-Hill composite failure model (Eq. (3)). The resulting optimal parameters determined from the fitting procedures are collected in Table 1.

Table 1
Output parameters from the apparent modulus (Eq. (2)) and yield stress (Eq. (3)) fit.

Compliance tensor	Axial elastic modulus (E_a)	27.65 *GPa*
	Transverse elastic modulus (E_t)	7.28 *GPa*
	Out-of-plane Poisson ratio (ν_a)	0.7
	In-plane Poisson ratio (ν_t)	0.3*
	Shear modulus (μ_a)	8.22
Tsai-Hill	Strength along axial direction *(X)*	318 *MPa*
	Strength along transverse direction *(Y)*	111 *MPa*
	Shear strength *(S)*	206 *MPa*

* – from [75]

3.3. Other parameters affecting microscale mechanical properties of bone

Besides MCF orientation, other factors like the degree of mineralization and overall variation in biochemistry may affect the mechanical properties of bone lamellae.

For all tested bovine osteons, a relative standard deviation of about 7 % was observed for the mineral to matrix ratio, which was not sufficient to detect a significant correlation with the mechanical parameters ($p = 0.6$ for both elastic modulus and yield stress). The relative standard deviation of mineral crystallinity did not exceed 1% and no significant correlation with the elastic modulus ($p = 0.3$) nor with the yield stress ($p = 0.2$) was observed. Although the Raman intensity ratio of amide I/ CH bending has been reported to quantify the relative concentrations of collagen versus NCPs [65], it was found to be strongly dependent on the sample orientation ($R^2 = 0.68$, $p < 0.01$). We therefore used the Raman intensity ratio of amide III/ CH bending instead to quantify the relative concentrations of collagen versus NCPs, as it showed a trend but no significant dependence on the collagen orientation ($p = 0.1$). Around 4 % of relative standard deviation of the collagen versus NCPs relative concentrations (amide III/ CH) was observed for the tested osteons. Moreover, a moderate dependence

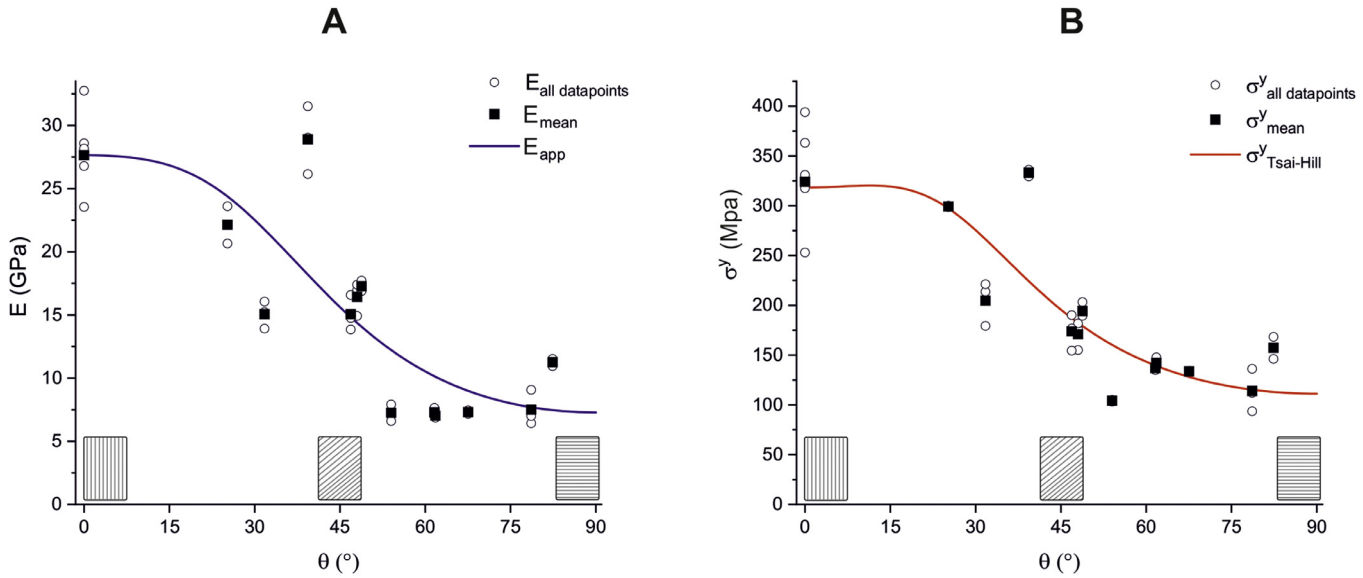

Figure 5. Elastic modulus and yield stress dependence on the collagen fibril out-of-plane orientation. The coefficients of determination R^2 are 0.50 and 0.61, respectively.

was found between the Raman intensity amide III/ CH ratio and the measured mechanical properties ($R^2 = 0.5$, $p = 0.01$ for both elastic modulus and yield stress). For further details, see Supplementary information C.

3.4. Post-yield behavior and failure modes

The stress-strain curves from the micropillar compression show softening for small MCF angles and hardening with the MCF orientations close to the transverse direction. To quantitatively analyze the softening/hardening behavior, the relative change of stress after the yielding point R was evaluated with the following ratio:

$$R = \frac{\left(\sigma^{pl} - \sigma^{y}\right)}{\sigma^{y}}, \tag{5}$$

where σ^{pl} signifies the stress value at the plateau region taken at 8% strain and σ^{y} is the yield stress (Figure 2 D). Negative values of the ratio correspond to strain softening and positive to hardening behavior, respectively. The transition between softening and hardening post-yield behavior was found for the MCF orientations at $\theta = 48^{\circ} - 54^{\circ}$, as marked in Figure 6. Relative change of stress after the yield point R (5) was then fitted with a hyperbolic tangent function (6), as it reflects well the behavior of the data.

$$R(\theta) = 0.21 \tanh\left(9.79(\theta - 49^{\circ})\right) - 0.10 \tag{6}$$

From the HRSEM images, different failure modes were encountered during compression tests: axial cracking (Figure 6 A), mushrooming (Figure 6 B), shear localization (Figure 6 C), homogeneous deformation (Figure 6 D) and a combination of above. As demonstrated in Figure 6, the majority of micropillars, which demonstrated softening behavior, failed in a localized shear crack, whereas those micropillars showing a hardening behavior deformed in a more homogeneous manner.

4. Discussion

The goal of this study was to assess the orientation dependent mechanical properties and deformation mechanisms of the basic building block of bone, the lamella. To this end, we developed and calibrated a procedure allowing to measure quantitatively the out-of-plane angle of MCF using qPRS with a high spatial resolution of ~0.3 μm^3. We then performed a large number of uniaxial compression experiments in hydrated conditions (N=36) on micropillars with known fibril orientation. Elastic modulus and yield stress were extracted and fitted using analytical models. Based on HRSEM images, the failure modes were identified as a function of fibril orientation. Finally, the post-yield behavior was extracted and related to the local fibril angle and observed failure mode. The different aspects of the study will be discussed in detail in the following paragraphs.

4.1. Quantitative Polarized Raman spectroscopy (qPRS)

qPRS is a non-invasive method for tissue composition and MCF orientation investigations with a high spatial resolution. In the past, it has been employed for quantitative analysis of MCF in-plane orientations [19]. Moreover, PRS was applied recently to resolve 3D orientation of MCF in rat tail tendons [17] and human cortical bone [16]. However, the reported studies on spatial MCF organization using PRS were mainly qualitative. To our knowledge, we are the first to report a method that allows applying PRS for quantitative estimation of bone MCF orientation in 3D. For this we performed PRS calibration on mineralized turkey leg tendon, a model material with highly aligned mineralized collagen fibrils, and validated it on bovine cortical bone.

Our calibration study followed the general methodology of Spiesz et al. [11], where a calibration function for quantifying MCF out-of-plane orientation was determined based on measurements performed on MTLT samples with a known uniaxial fiber orientation. Polarized light microscopy is a relatively fast and well-known technique, however it requires thin sample cuts at a fixed thickness over which the signal is integrated. This can pose significant problems if osteons are not oriented parallel to the light beam. In the present study, the application of PRS gives us significant advantage in the spatial resolution, since we use a confocal system and collect the signal from a ~0.3 μm^3 volume. In case of bovine cortical bone osteons with lamellar thickness of several microns, the Raman focal volume is small enough to collect information from locally aligned MCF. Even in the case of human cortical bone osteons, where each lamella (thickness ~7 μm) is composed of several sub-lamellae (thickness ~1 μm) [50], the resolution should be sufficient to supply information on the local MCF orientation, even

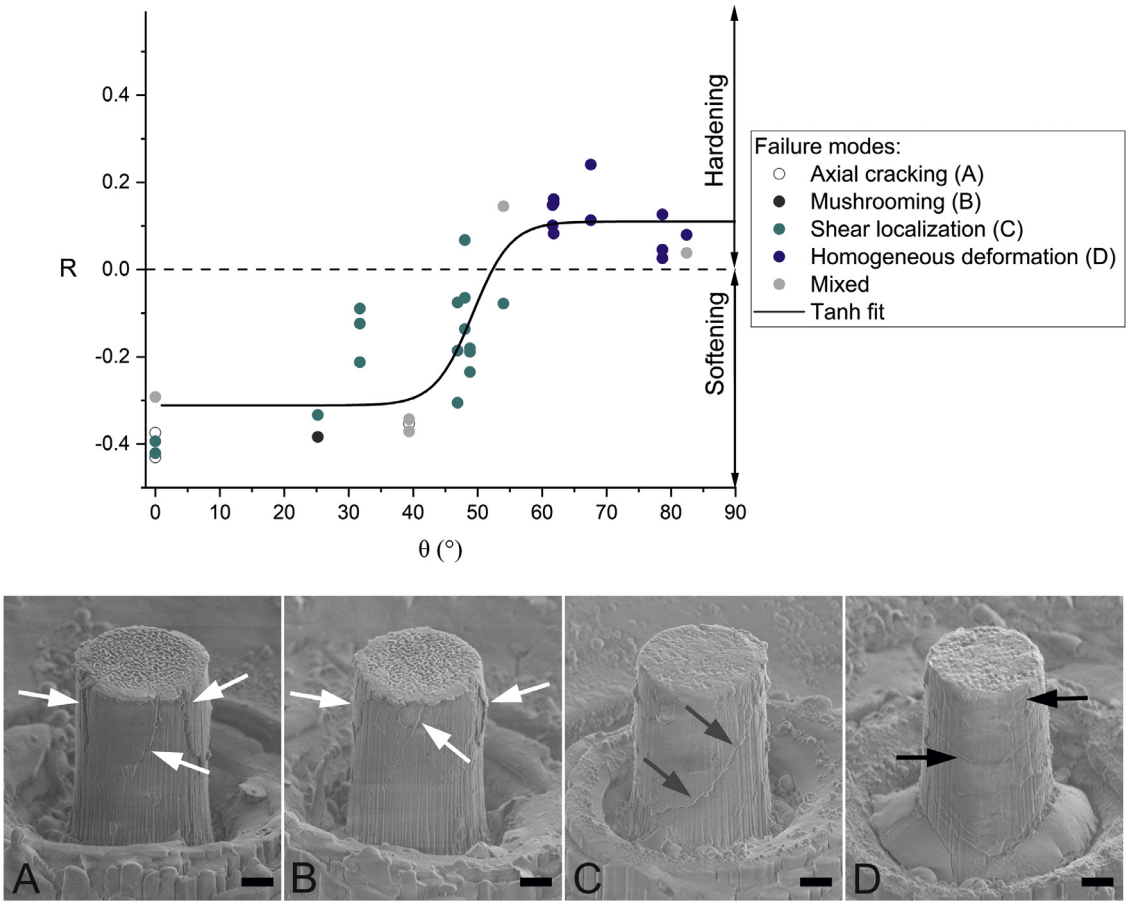

Figure 6. Post-yield behavior and failure modes encountered in compression tests of micropillars with different out-of-plane MCF angles θ. Failure modes were analyzed visually based on HRSEM images, the representative HRSEM images of each failure mode with marked stress concentration regions are shown at the bottom (white arrows point to the vertical cracks, grey arrows point to the oblique cracks, and black arrows point to the horizontal cracks). Softening/hardening behavior was estimated from the relative change of stress after the yielding point R (Eq. (5)) and fitted with hyperbolic tangent function (Eq. (6)). The coefficient of determination R^2=0.72, scale bar 1 μm.

though some averaging effects are likely to occur when the sample is misaligned with the laser beam [16].

In comparison with other available methods of MCF spatial orientation analysis, such as SAXS/WAXS and nanoCT, qPRS does not expose the sample to a high energy X-ray beam. With the qPRS parameters used throughout this work, no structural modifications of the sample were observed (Supplementary information B.4). Moreover, qPRS does not require additional time-consuming sample preparation, as in the case of e.g. TEM imaging [14]. The spatial resolution of qPRS is defined by the Raman setup, for example the objective numerical aperture or the incident laser wavelength. In this study, the focal spot size was estimated to be ~0.4 μm in diameter, which is suitable for the lamellar scale investigations.

PRS measurements on MTLT were in good agreement with the theoretical prediction (Figure 1 and Supplementary information B.1). The function from the theoretical prediction (equation S8, Supplementary information B.2) was found to be not suitable for the MCF angle θ extraction due to the interdependency of the output parameters. We therefore used a simplified fitting function (1) following the methodology proposed by Bao et al. [59] to extract the output Raman parameters, including the parameter of anisotropy A/B. The simplified fit precision was comparable to the theoretical prediction (for both, $R^2 > 0.99$). The angular uncertainty of the qPRS method $\theta^{err} = 9.7^\circ$ (Supplementary information B.5). While this error is not negligible, the application to bovine bone showed that the method is precise enough to extract meaningful data for studying microscale structure-property relationships.

Prior to the validation study on bovine cortical bone, polarized Raman line maps were collected on three bovine bone osteons to quantify the variation of fibril orientation within each osteon (Supplementary information B.3). The out-of-plane MCF angle θ, averaged across the osteon, was different from the micro-CT measurements: 11±9° for the 6° osteon and 8±7° for the 4° osteon, resulting in an average disagreement of 4-5° between the different methods. This is well below the angular uncertainty of both methods and therefore may be neglected. On average, a standard deviation of ±7° was found for the MCF alignment within each osteon. Again, as this standard deviation is below the experimental uncertainty of the proposed qPRS procedure for fibril out-of-plane angle estimation, it may be neglected. Therefore, we collected only one set of 19 polarized Raman spectra per osteon.

Micro-CT scans were used for osteonal orientation determination. With ~5 μm resolution, this technique is suitable to locate the Haversian canals together with osteonal and interstitial zones of cortical bone, but does not have sufficient contrast and resolution to distinguish between individual bone lamellae. Osteonal angle, as determined from micro-CT, was used to screen the osteons on each sample to reach a homogeneous distribution of fibril orientations and to cross validate with qPRS.

Previously reported PRS studies on bone employed another experimental design using an additional analyzer plate in the path of the scattered light. There, the theoretical dependence of the Raman scattering on light polarization was calculated from four experimental configurations of polarizer/analyzer parallel and orthogonal alignments [19,76]. In more recent works [16–18], the collection of

the scattered light for a range of incoming laser polarization angles was proposed. In the present study, we established a method for quantitative estimation of MCF spatial orientation by determining a calibration function between polarization anisotropy and MCF out-of-plane angle on mineralized turkey leg tendon, a model material with a very similar composition and ultrastructure to bone featuring highly aligned collagen fibrils. The approach proposed in this study requires a higher number of measurements than the former, however, it increases the robustness and accuracy, as the collected scattered light has higher intensities due to the absence of an analyzer leading to an increased signal to noise ratio (SNR). Furthermore, the influence of data scatter due to natural variability and experimental artefacts is reduced due to the employed fitting procedure, which analyzes the best fit of many experiments rather than relying on the direct determination of the Raman tensor from a limited number of measurements, which is more sensitive to experimental artefacts.

In this work, the newly proposed qPRS method is used to evaluate the orientation of collagen fibers based on polarization dependence of amide Raman bands. However, alternative polarization dependent Raman bands may be used. We specifically acknowledge the possibility to use the amide I/ ν_2PO_4 for MCF orientation estimation, following the same spectra acquisition and data processing protocols. Detailed analysis is presented in the Supplementary information B.6. We demonstrate an excellent correlation between the two Raman band integrated intensity ratios for MTLT samples (R^2=0.98, p = 0.01). Moreover, we calibrated the anisotropy parameter A/B, extracted from amide I/ ν_2PO_4 polarization dependence, with the fibril out-of-plane angle θ, taken from the SAXS measurements (R^2 = 0.99). Consequently, the parameters of the calibration function for amide I/ ν_2PO_4 (Eq. (4)) are: C_0=1.09, C_2=-0.05 and C_4=0.76. These parameters can be used as an alternative for estimating the out-of-plane MCF angle based on local measurement of amide I/ ν_2PO_4 Raman band integrated intensity ratios. In the present work, all of the collected spectra had a high background fluorescence, overlapping with the ν_2PO_4 band intensity, as can be seen, for example, from the raw spectra presented in the Supplementary information B.1. We therefore chose to use the amide I and amide III bands for the qPRS method, as they both were not affected by the sample fluorescence.

Besides MCF orientation, we also investigated the effects of mineral to matrix ratio, mineral crystallinity, and relative NCP content of the bovine cortical bone osteons. All of these parameters have a low relative standard deviation, which indicates the homogeneity of the tested tissue.

A clear limitation of the proposed method is related to the isotropy of the polarization response of both axially aligned and randomly oriented fibrils. As no polarization dependence exists for the integral area ratio of the collagen peaks of interest, special care needs to be taken to distinguish between these two types of fibril orientations. We have not encountered such a situation during this study, as we used model bone materials with a simplified, mostly uniaxially aligned microstructure. For future measurements, we propose, as a possible remedy, to collect additional spectra while tilting the sample by a known angle or to include amide I intensity into the analysis.

4.2. Mechanical testing

Here, we performed for the first time microscale compression experiments on the length scale of single bone lamellae in hydrated state for a broad spectrum of known local fibril orientations. The elastic modulus and strength nonlinearly decreased with the increasing MCF angle. The theory of linear elasticity for transversely isotropic materials and Tsai–Hill criterion were found to describe well the variation of these properties with the fiber orientation (Figure 5). The found non-linear behavior as a function of MCF angle on the single lamella level of bone is comparable to what has been observed in other short fiber reinforced polymer composites [77]. In the majority of previously reported studies, the microscale mechanical properties of bone were investigated for two assumed MCF orientations: axial ($\theta = 0°$) and transverse ($\theta = 90°$). However, no means of quantification of the true fibril angles existed. Here, the mechanical compression experiments were performed on bone lamellae with 13 known MCF orientations in the range from 0° to 82° (Figure 5). This provides a unique dataset for identifying the structure-property relationships of bone on the lamellar scale through a combination of micropillar compression and MCF orientation determination using non-invasive qPRS.

Fibril misalignment is a common phenomenon for natural materials, such as bone, and it significantly affects the accuracy of measured mechanical parameters. When it comes to clinical investigations of bone strength as a function of age, gender, disease, or treatment, it becomes especially important to separate the respective contributions of macroscopic bone geometry and density, which are clinically assessed today [78], from the intrinsic tissue properties that depend on microstructural factors, like local degree of mineralization or fibril orientation distribution [79]. Multiscale structural organization and mechanical property analysis of bone biopsies may be used in the future for studying the changes in tissue organization and mechanical properties related to bone metabolic diseases like osteoporosis [5,10,80]. In preclinical osteoporosis and bone research, different large and small animal models are used as a model for human bone [81,82]. For different species (e.g. human, canine, mice) the collagen fibrils in osteonal lamellae have been reported to feature an offset angle with respect to the bone's long axis in a range of 20-30° [11,19,50,83]. In this study, a variation of the MCF out-of-plane orientation of up to 16° was observed within the osteonal regions of the bovine cortical bone sample. This variation in fibril orientation is an intrinsic property of bone in different species that leads to considerable data scatter in mechanical experiments and warrants further investigation. Especially when analyzing micromechanical experiments, it is of high interest to employ methods for quantifying the local MCF orientation and degree of mineralization in the region of interest to reduce apparent data scatter and identify structure-property relationships with high fidelity.

As expected from the micropillar compression experiments, the highest value of elastic modulus was found for the axial MCF orientation ($E_a = 27.65\ GPa,\ \theta = 0°$) and the lowest for transverse orientations ($E_t = 7.28\ GPa,\ \theta > 60°$). This tendency is in good agreement with previously reported data on the mechanical experiments on bone, collected in Table 2. The axial elastic modulus value is greater than the majority of values reported in literature for both micro- ($21 - 23\ GPa$, [84–86]) and macro-scale compression experiments ($\sim 20\ GPa$, [87,88]). The first may be due to the natural variations in MCF orientation in cortical bone specimen that has been shown to be present in different species [11,19,50,83]. As previous studies on microscale cortical bone mechanical properties did not verify the MCF orientation, the reported data is likely averaged over a MCF misorientation range of up to 30°, which can explain the reported lower average elastic modulus values. At the macroscale, the mechanical response is averaged over large regions with different degrees of mineralization and fibril orientation and includes the effect of Haversian porosity, therefore also from these experiments a lower apparent modulus can be expected [89].

The measured transverse elastic modulus is lower than the previously reported values from both macro- and micro-scale mechanical tests on bovine bone [87,88,90,91]. This leads to higher elastic anisotropy values ($E_a/\ E_t$), compared to previously reported data

Table 2
Reported mechanical anisotropy values and experimental details.

Elastic anisotropy values	Plastic anisotropy values	Characteristic specimen size	Conditions	Method	Sample	Ref.
$\frac{27.7}{7.3} = 3.8$	$\frac{0.33}{0.13} = 2.54$	5 μm	Hydrated, >93% rh	Compression	Bovine	Present work
$\frac{19.1(\pm2.8)}{11.6(\pm2.4)} = 1.6$	$\frac{0.18(\pm0.02)}{0.11(\pm0.02)} = 1.64$	5 mm	Ambient	Compression	Bovine	[87]
$\frac{20.5(\pm2.3)}{13.0(\pm2.3)} = 1.6$	$\frac{0.18(\pm0.02)}{0.16(\pm0.01)} = 1.13$	5 mm	Ambient	Compression	Bovine	[88]
$\frac{26.9}{22.6} = 1.2$ $\frac{26.9}{18.0} = 1.5$		350 nm	Ambient	Indentation	Bovine	[90]
$\frac{27.5(\pm2.2)}{19.0(\pm1.8)} = 1.5$	$\frac{1.01(\pm0.13)}{0.67(\pm0.08)} = 1.51$	7 μm	Ambient	Indentation	Ovine	[38]
$\frac{22.8(\pm1.6)}{14.5(\pm1.6)} = 1.6$	$\frac{0.60(\pm0.11)}{0.51(\pm0.08)} = 1.18$	7 μm	Hydrated, liquid immersion	Indentation	Ovine	[38]
$\frac{31.2(\pm6.5)}{16.5(\pm1.5)} = 1.9$	$\frac{0.50(\pm0.10)}{0.30(\pm0.02)} = 1.63$	5 μm	*in vacuo*	Compression	Ovine	[38]
	$\frac{0.17(\pm0.02)}{0.13(\pm0.03)} = 1.31$	5 μm	Hydrated, liquid immersion	Compression	Ovine	[32]
$\frac{13.7(\pm0.8)}{6.5(\pm1.0)} = 2.1$		17.5 μm	Ambient	Indentation	MTLT	[47]
$\frac{18.1(\pm2.9)}{10.2(\pm1.8)} = 1.8$		6.3 μm	Ambient	Indentation	MTLT	[47]
$\frac{12.9(\pm1.6)}{2.9(\pm0.9)} = 4.5$		17.5 μm	Hydrated	Indentation	MTLT	[47]
$\frac{30.2(\pm4.1)}{17.6(\pm1.9)} = 1.75$		1.8 μm	Ambient	Indentation	Human	[102]
$\frac{24.7(\pm2.7)}{17.3(\pm1.9)} = 1.4$ $\frac{24.7(\pm2.7)}{9.2(\pm0.6)} = 2.7$		5.6 μm	Ambient	Indentation and orthotropic stiffness tensor model [103]	Human	[104]

Elastic anisotropy values: $\frac{E_a}{E_t}$; plastic anisotropy values: $\frac{H_a}{H_t}$ for indentation and $\frac{\sigma_a^y}{\sigma_t^y}$ for compression tests; all reported mechanical values are in GPa; characteristic specimen size calculated as $7 * (penetration\ depth)$for indentation, pillar diameter for compression.

in the literature (Table 2). This could be related to the fact that we are testing bundles of aligned collagen fibrils in the transverse direction, a situation not encountered during macroscopic experiments, where the tested volume contains a variety of fibril orientations. It should be noted, however, that our setup is likely prone to sample surface swelling artifacts in hydrated conditions. Similar behavior was already reported for hydrated ovine [32,38], bovine [31] and MTLT [47] samples, where observed anisotropy ratios increased up to 2.5 times in comparison to dry experiments. Such anisotropic response to hydration might be a result of MCF structural changes. As was shown by Andriotis et al. [92], during single collagen fibril hydration, the stiffness will exhibit a fourfold higher reduction in transverse direction than in the axial direction, due to the different collagen packing density. In micropillars with fibrils aligned in axial orientation, the surrounding fibrils enforce a constraint on radial fibril swelling, therefore this effect is diminished. However, in transverse specimens, the radial swelling of fibrils at the top surface is not inhibited, which could lead to substantial artifacts in the mechanical measurements, as these surface fibrils are likely to be significantly more compliant and, from a mechanical perspective, arranged in series with the remaining micropillar.

In this work, the yield stress values measured in both axial and transverse directions ($\sigma_a^y = 329.97\ MPa,\ \sigma_t^y = 131.63\ MPa$) are higher than previously reported from macroscale compression tests [87,88]. When compared to experiments performed on the same characteristic specimen size (5 µm) on ovine cortical bone lamella, the values are also higher than those from hydrated tests in buffered solution [32] but lower than the data obtained *in vacuo* [38]. Overall, bone hydration is one of the important parameters affecting bone mechanical properties [93,94]. In our study, the bone samples were measured in a humidified atmosphere, with relative humidity above 93% to mimic physiological conditions. Prior to the measurements, samples were kept in a hydrated atmosphere for at least 4 h, to ensure the sample equilibration. We verified that the measured values of the elastic modulus and yield stress were constant within each day of experiments (see Supplementary information F.2) therefore assuring that the specimens had reached an equilibrated hydration state prior to the measurements. We assume that the micropillar swelling affects the measured yield stress, as the micropillar geometry, used for stress and strain calculations, was assessed prior to mechanical testing. For future mechanical testing it is recommended to estimate the swelling effects on specimen geometry in humidified atmosphere. For this, high-resolution techniques, such as environmental SEM [95], atomic force microscopy [92] or SAXS [96] could be used.

Remarkably, the yield stress values observed for the MCF orientations from 0° and up to 25° are nearly constant. This was also reported for microscale tensile and compressive strength modelling of ovine cortical bone [34]. Such tolerance to the MCF small angle variations is in line with the natural variability in MCF orientation

found in different species [11,19,50,83], which could act as one of the bone's toughening mechanisms [97,98].

Besides MCF orientation, osteonal bone lamellation and overall variation in biochemistry may affect microscale mechanical properties of bone. In present study, the degree of mineralization and the mineral crystallinity did not show significant correlations with the mechanical data due to their small respective variations. However, we found a weakly significant dependence of the observed mechanical properties with variations of collagen/ NCPs relative concentrations. Indeed, the spatial arrangement of NCPs within bone matrix may determine bone's mechanical properties including toughness [99–101]. It is therefore recommended to include alternative analysis methods for NCPs content and biochemistry screening for the future studies on bone microscale mechanical properties. Moreover, structural inhomogeneity in the volume of a single micropillar may be introduced due to the lamellar structure of osteonal bone. As was experimentally verified by Raman line scans taken in several osteons on the bovine bone specimen, MCF were highly aligned with the osteon axis with a standard deviation of 7° (Supplementary information B.3) in contrast to the 30° average variation, that has been observed in human secondary osteons [50]. This suggests that the osteonal bone in our bovine specimen consisted mainly of primary osteons with highly aligned MCF uniaxially oriented in the osteon direction in each lamella.

4.3. Post-yield behavior and failure modes

As demonstrated in this study, post-yield behavior and failure modes of bone micropillars depend on MCF orientation. According to the stress-strain curves from the microcompression experiments (Figure 4 A), a clear strain softening is observed for the MCF close to axial orientation and strain hardening for transverse MCF orientations. The same was observed in previously reported micropillar compression experiments on ovine cortical bone [32,33]. Closer examination of the post-yield behavior (Figure 6) revealed two plateau regions of the relative change in stress ratio (Eq. (5)). The first one corresponds to the softening observed at lower MCF angles ($\theta < 30^\circ$). Interestingly, this plateau in softening ratio also coincides with the range of constant yield stress, demonstrating that the inelastic behavior of bone lamellae remains mostly unchanged for misalignment angles below 30°. The second plateau at higher MCF angles ($\theta > 50^\circ$) resembles post-yield hardening behavior. For the intermediate MCF angles, a steep change from softening to hardening is observed, featuring a transition not only in the post-yield behavior, but also in the failure mode, which suggests a change in deformation mechanisms between axial and transverse specimens.

The structural complexity of bone leads to hierarchical and coupled deformation mechanisms (fibril - extrafibrillar matrix, mineral - collagen) down to the nanoscale [105]. A variety of failure modes occurred at $\theta \in (0^\circ, 50^\circ)$. At the angles close to axial ($0^\circ < \theta < 25^\circ$), MCF orientation is moderately aligned with the loading direction and most of the load is carried by the fibrils. In this case, axial cracking along the length of the pillars (Figure 6A) or localization at the top of the pillars (mushrooming, Figure 6 B) is observed. The proposed deformation mechanism that could be directly tuned by the MCF misalignment with the loading direction is the fibril-extrafibrillar matrix (EFM) interfacial sliding [100]. Such deformation occurs due to interface failure between fibrils, e.g. axial cracking along the length of the pillars or mushrooming. Similar damage behavior for axially aligned MCF was observed in the work of S. Li et al. [87]. When the bone is compressed beyond the yield point, critical interfacial shear strength between the fibril and the matrix is exceeded. When this happens, matrix flows past the fibrils, resulting in frictional losses and de-bonding of the fibrils and extrafibrillar matrix [100]. The thin fibril-EFM interface then flows past the fibrils, resulting in frictional losses, similar to the shear lag model for tensile loadings [106,107].

With the increase in MCF angle, localized shear cracks are observed. Interestingly, at the lower angles of MCF, the shear plane was steeper than at higher angles, which suggests the existence of a correlation between the MCF and shear plane orientations. This is in line with the notion of fibril-EFM interface failure for angles below 50°. For MCF orientations $\theta > 50^\circ$, the main failure mode occurring in this work is homogeneous deformation. We believe that when the MCF angles reach the softening threshold of 48°-54°, the shear load applied to the tilted fibril-matrix interface is not sufficient to cause deformation in localized shear zones, due to the high normal force and, therefore, an increased frictional component. The deformation is assumed to happen in the extrafibrillar matrix and homogeneously spread throughout the pillar volume, which is compacted so that frictional hardening occurs. Moreover, the nanogranular friction from mineral-mineral interparticle interactions may additionally influence the post-yield bone deformation mechanisms, especially in compression. As was shown in the work of Tai et al [108], at the nanoscale, bone exhibits a pressure sensitive plasticity. Similar to other nanogranular materials, bone features a nanoscale porosity [109,110], which leads to a plastic contraction under compressive loading. This, together with the fibril-extrafibrillar interfacial sliding, would lead to a cohesive frictional sliding with tunable softening/hardening behavior depending on the shear flow instabilities.

4.4. General limitations

The techniques used in this study analyze different volumes of interest. qPRS provides structural and compositional information from ~0.3 μm^3 volume. For both MTLT and bovine cortical bone lamellae, such volume would include several MCFs. At the same time, SAXS beam size at sample position was about 400 μm in diameter, which integrates over thousands of MCFs. However, we could combine these two techniques on the MTLT sample because of its extremely aligned ultrastructure, made up of densely packed MCF, therefore locally and globally the orientations are highly correlated [45–47].

In this study we combined qPRS and micropillar compression on bovine cortical bone samples. While qPRS gives structural information on the length scale of several MCF, the latter provides mechanical data on the lamellar scale (characteristic micropillar size 5 µm). However, we could show experimentally by Raman line scans taken in several osteons on the bovine bone specimen that MCFs in primary bovine osteons are highly aligned with the osteon axis (7° standard deviation) and that no plywood-like variation in MCFs was present (Supplementary information B.3). It was furthermore verified that there is a clear correlation between osteonal and MCF angles (Fig. 3 B). This, together with the low scatter in the collected mechanical data for different MCF orientations, suggests a well aligned MCFs arrangement as determined by qPRS. We therefore assume that the tested micropillars were made up of homogeneously aligned MCFs, which is corroborated by our findings. In the future studies, when applying these techniques to a tissue with a more complicated microstructure such as human lamellar bone, care has to be taken to better match the tested volumes of the two methods, e.g. by scanning the focal spot through the micropillar and acquiring several qPRS measurements. qPRS was not performed on each micropillar in this study because of the incompatible specimen fabrication steps. In order to fabricate micropillars on the bone surface the sample needs to be sputtered with conductive material (Au, 11 nm), which reflects the incoming laser beam and therefore significantly decreases the spectrum quality. Therefore, MCF orientation was measured before micropillar production in each osteon. As we found that MCFs are highly

aligned and show little variation within an osteon, we could correlate the micromechanical properties to the average MCF orientation. However, for future studies combining these two methods on more complex tissues like human bone, another method should be used for micropillar preparation. A suitable approach would be employing femtosecond laser ablation [111], which does not require sputtering of a conductive film and therefore results in specimens suitable for local qPRS measurements.

5. Conclusion

The focus of this study was to investigate the effect of local microstructure, especially MCF orientation, on the microscale mechanical properties of isolated bone lamellae. In order to achieve this, a polarized Raman spectroscopy based method was developed that allows measuring local MCF angle with an angular uncertainty $<10°$. The combination of polarized Raman spectroscopy and micropillar compression made it possible to detect changes in mechanical properties with the MCF angle. This allowed us to measure a unique spectrum of microscale mechanical compression data for MCF orientations ranging from 0° to 82°. We could demonstrate a strong dependence of the microscale compressive mechanical properties of bone on the MCF orientations. On the other hand, the degree of mineralization and the mineral crystallinity did not show significant correlations with the mechanical data due to their small respective variations. A high degree of anisotropy was found for both the elastic modulus ($E_a/E_t = 3.80$) and the yield stress ($\sigma_a^y/\ \sigma_t^y\ = 2.54$). Moreover, the post-yield behavior was found to depend on the MCF orientation with a transition between softening to hardening at $\theta = 48^\circ - 54^\circ$. Measuring the local microstructural (such as MCF angle, mineralization) and mechanical properties in a site-matched fashion allowed us to reduce the apparent scatter in the collected mechanical data and to reliably determine structure-property relationships of bone at the lamellar level. This is a prerequisite for developing and validating multiscale models predicting bone failure in the future.

Declaration of Competing Interest

The authors declare no competing financial interests.

Acknowledgements

This work is funded by the Special Focus Area Personalized Health and Related Technologies (SFA PHRT) iDoc Project 2017-304 (TK), Swiss National Science Foundation (SNSF) Ambizione grant no. 174192 (CP and JS) and SNSF project no. 173012 (AKM and AN). The authors wish to thank B. Voumard for the help during the sample preparation, D. Casari for the FIB guidelines, M. Indermaur for the micro-CT guidelines and R. Muff for technical support during the automatization of the polarization dependent Raman measurements.

Supplementary materials

Supplementary material associated with this article can be found, in the online version, at doi:10.1016/j.actbio.2020.10.034.

References

[1] P. Barry, T. Aspray, K. Briers, G. Collins, J. Compston, F. Dockery, S. Ruddick, P. Selby, D. Stephens, A. Thornhill, J. Tobias, Osteoporosis : fragility fracture risk, Natl. Inst. Heal. Clin. Excell (2012) 1–97 http://www.ncbi.nlm.nih.gov/pubmed/23285503.

[2] F. Borgström, L. Karlsson, G. Ortsäter, N. Norton, P. Halbout, C. Cooper, M. Lorentzon, E.V. McCloskey, N.C. Harvey, M.K. Javaid, J.A. Kanis, J.Y. Reginster, S. Ferrari, Fragility fractures in Europe: burden, management and opportunities, Arch. Osteoporos 15 (2020) https://doi.org/10.1007/s11657-020-0706-y.

[3] K. Engelke, T. Lang, S. Khosla, L. Qin, P. Zysset, W.D. Leslie, J.A. Shepherd, J.T. Schousboe, Clinical Use of Quantitative Computed Tomography (QCT) of the Hip in the Management of Osteoporosis in Adults: the 2015 ISCD Official Positions—Part I, J. Clin. Densitom. 18 (2015) 338–358 https://doi.org/10.1016/j.jocd.2015.06.012.

[4] S. Bailey, D. Vashishth, Mechanical Characterization of Bone: State of the Art in Experimental Approaches—What Types of Experiments Do People Do and How Does One Interpret the Results? Curr. Osteoporos. Rep. 16 (2018) 423–433 https://doi.org/10.1007/s11914-018-0454-8.

[5] M.J. Mirzaali, J.J. Schwiedrzik, S. Thaiwichai, J.P. Best, J. Michler, P.K. Zysset, U. Wolfram, Mechanical properties of cortical bone and their relationships with age, gender, composition and microindentation properties in the elderly, Bone 93 (2016) 196–211 https://doi.org/10.1016/j.bone.2015.11.018.

[6] J.Y. Rho, L. Kuhn-Spearing, P. Zioupos, Mechanical properties and the hierarchical structure of bone, Med. Eng. Phys. 20 (1998) 92–102 https://doi.org/10.1016/S1350-4533(98)00007-1.

[7] J.D. Currey, Bones: Structure and mechanics, 2013.

[8] N. Reznikov, R. Shahar, S. Weiner, Bone hierarchical structure in three dimensions, Acta Biomater 10 (2014) 3815–3826 https://doi.org/10.1016/j.actbio.2014.05.024.

[9] I. Jimenez-Palomar, A. Shipov, R. Shahar, A.H. Barber, Structural orientation dependent sub-lamellar bone mechanics, J. Mech. Behav. Biomed. Mater 52 (2015) 63–71 https://doi.org/10.1016/j.jmbbm.2015.02.031.

[10] M. Georgiadis, R. Müller, P. Schneider, Techniques to assess bone ultrastructure organization: Orientation and arrangement of mineralized collagen fibrils, J. R. Soc. Interface 13 (2016) https://doi.org/10.1098/rsif.2016.0088.

[11] E.M. Spiesz, W. Kaminsky, P.K. Zysset, A quantitative collagen fibers orientation assessment using birefringence measurements : Calibration and application to human osteons, J. Struct. Biol. 176 (2011) 302–306 https://doi.org/10.1016/j.jsb.2011.09.009.

[12] R. Genthial, E. Beaurepaire, M.C. Schanne-Klein, F. Peyrin, D. Farlay, C. Olivier, Y. Bala, G. Boivin, J.C. Vial, D. Débarre, A. Gourrier, Label-free imaging of bone multiscale porosity and interfaces using third-harmonic generation microscopy, Sci. Rep 7 (2017) 1–16 https://doi.org/10.1038/s41598-017-03548-5.

[13] A. Golaraei, K. Mirsanaye, Y. Ro, S. Krouglov, M.K. Akens, B.C. Wilson, V. Barzda, Collagen chirality and three-dimensional orientation studied with polarimetric second-harmonic generation microscopy, J. Biophotonics 12 (2019) 1–9 https://doi.org/10.1002/jbio.201800241.

[14] M.A. Rubin, I. Jasiuk, J. Taylor, J. Rubin, T. Ganey, R.P. Apkarian, TEM analysis of the nanostructure of normal and osteoporotic human trabecular bone, Bone 33 (2003) 270–282 https://doi.org/10.1016/S8756-3282(03)00194-7.

[15] A. Groetsch, A. Gourrier, J. Schwiedrzik, M. Sztucki, R.J. Beck, J.D. Shephard, J. Michler, P.K. Zysset, U. Wolfram, Compressive behaviour of uniaxially aligned individual mineralised collagen fibres at the micro- and nanoscale, Acta Biomater (2019) https://doi.org/10.1016/j.actbio.2019.02.053.

[16] S. Schrof, P. Varga, L. Galvis, K. Raum, A. Masic, 3D Raman mapping of the collagen fibril orientation in human osteonal lamellae, J. Struct. Biol. 187 (2014) 266–275 https://doi.org/10.1016/j.jsb.2014.07.001.

[17] L. Galvis, J.W.C. Dunlop, G. Duda, P. Fratzl, A. Masic, Polarized Raman Anisotropic Response of Collagen in Tendon: Towards 3D Orientation Mapping of Collagen in Tissues, PLoS One 8 (2013) 1–9 https://doi.org/10.1371/journal.pone.0063518.

[18] S. Gamsjaeger, A. Masic, P. Roschger, M. Kazanci, J.W.C. Dunlop, K. Klaushofer, E.P. Paschalis, P. Fratzl, Cortical bone composition and orientation as a function of animal and tissue age in mice by Raman spectroscopy, Bone 47 (2010) 392–399 https://doi.org/10.1016/j.bone.2010.04.608.

[19] M. Raghavan, N.D. Sahar, R.H. Wilson, M.-A. Mycek, N. Pleshko, D.H. Kohn, M.D. Morris, Quantitative polarized Raman spectroscopy in highly turbid bone tissue, J. Biomed. Opt. 15 (2010) 037001 https://doi.org/10.1117/1.3426310.

[20] R.B. Martin, J. Ishida, The relative effects of collagen fiber orientation, porosity, density, and mineralization on bone strength, J. Biomech 22 (1989) 419–426 https://doi.org/10.1016/0021-9290(89)90202-9.

[21] H. Oxlund, M. Barckman, G. Ørtoft, T.T. Andreassen, Reduced concentrations of collagen cross-links are associated with reduced strength of bone, Bone 17 (1995) 365–371 https://doi.org/10.1016/8756-3282(95)00328-B.

[22] P. Zioupos, J.D. Currey, A.J. Hamer, The role of collagen in the declining mechanical properties of aging human cortical bone., J. Biomed. Mater. Res. 45 (1999) 108–116 https://doi.org/10.1002/(sici)1097-4636(199905)45:2⟨108::aid-jbm5⟩3.0.co;2-a.

[23] X. Wang, R.A. Bank, J.M. TeKoppele, C. Mauli Agrawal, The role of collagen in determining bone mechanical properties, J. Orthop. Res. 19 (2001) 1021–1026 https://doi.org/10.1016/S0736-0266(01)00047-X.

[24] J.S. Nyman, A. Roy, X. Shen, R.L. Acuna, J.H. Tyler, X. Wang, The influence of water removal on the strength and toughness of cortical bone, J. Biomech 39 (2006) 931–938 https://doi.org/10.1016/j.jbiomech.2005.01.012.

[25] M. Unal, O. Akkus, Raman spectral classification of mineral- and collagen-bound water's associations to elastic and post-yield mechanical properties of cortical bone, Bone 81 (2015) 315–326 https://doi.org/10.1016/j.bone.2015.07.024.

[26] P. Ammann, R. Rizzoli, Bone strength and its determinants, Osteoporos. Int. 14 (Suppl 3) (2003) 13–18 https://doi.org/10.1007/s00198-002-1345-4.

[27] A. Sheu, T. Diamond, Bone mineral density: Testing for osteoporosis, Aust. Prescr. 39 (2016) 35–39 https://doi.org/10.18773/austprescr.2016.020.

[28] W.T. Dempster, R.T. Liddicoat, Compact bone as non-isotropic material, Am. J. Anat. 91 (1952) 331–362.

[29] A. Ascenzi, E. Bonucci, The compressive properties of single osteons, Anat. Rec. 161 (1968) 377–391 https://doi.org/10.1002/ar.1091610309.
[30] A. Ascenzi, E. Bonucci, The tensile properties of single osteons, Anat. Rec 158 (1967) 375–386 https://doi.org/10.1002/ar.1091580403.
[31] J. Seto, H.S. Gupta, P. Zaslansky, H.D. Wagner, P. Fratzl, Tough lessons from bone: Extreme mechanical anisotropy at the mesoscale, Adv. Funct. Mater 18 (2008) 1905–1911 https://doi.org/10.1002/adfm.200800214.
[32] J. Schwiedrzik, A. Taylor, D. Casari, U. Wolfram, P. Zysset, J. Michler, Nanoscale deformation mechanisms and yield properties of hydrated bone extracellular matrix, Acta Biomater 60 (2017) 302–314 https://doi.org/10.1016/j.actbio.2017.07.030.
[33] J. Schwiedrzik, R. Raghavan, A. Bürki, V. Lenader, U. Wolfram, J. Michler, P. Zysset, In situ micropillar compression reveals superior strength and ductility but an absence of damage in lamellar bone, Nat. Mater 13 (2014) 740–747 https://doi.org/10.1038/nmat3959.
[34] D. Casari, J. Michler, P. Zysset, J. Schwiedrzik, Microtensile properties and failure mechanisms of cortical bone at the lamellar level, Acta Biomater (2020) https://doi.org/10.1016/j.actbio.2020.04.030.
[35] J.Y. Rho, T.Y. Tsui, G.M. Pharr, Elastic properties of human cortical and trabecular lamellar bone measured by nanoindentation, Biomaterials 18 (1997) 1325–1330 https://doi.org/10.1016/S0142-9612(97)00073-2.
[36] P.K. Zysset, X. Edward Guo, C. Edward Hoffler, K.E. Moore, S.A. Goldstein, Elastic modulus and hardness of cortical and trabecular bone lamellae measured by nanoindentation in the human femur, J. Biomech 32 (1999) 1005–1012 https://doi.org/10.1016/S0021-9290(99)00111-6.
[37] S.P. Lake, K.S. Miller, D.M. Elliott, L.J. Soslowsky, Effect of fiber distribution and realignment on the nonlinear and inhomogeneous mechanical properties of human supraspinatus tendon under longitudinal tensile loading, J. Orthop. Res. 27 (2009) 1596–1602 https://doi.org/10.1002/jor.20938.
[38] J. Schwiedrzik, R. Raghavan, A. Bürki, V. Lenader, U. Wolfram, J. Michler, P. Zysset, In situ micropillar compression reveals superior strength and ductility but an absence of damage in lamellar bone, Nat. Mater 13 (2014) 740–747 https://doi.org/10.1038/nmat3959.
[39] K.W. Luczynski, A. Steiger-Thirsfeld, J. Bernardi, J. Eberhardsteiner, C. Hellmich, Extracellular bone matrix exhibits hardening elastoplasticity and more than double cortical strength: Evidence from homogeneous compression of non-tapered single micron-sized pillars welded to a rigid substrate, J. Mech. Behav. Biomed. Mater. 52 (2015) 51–62 https://doi.org/10.1016/j.jmbbm.2015.03.001.
[40] O.A. Tertuliano, J.R. Greer, The nanocomposite nature of bone drives its strength and damage resistance, Nat. Mater 15 (2016) 1195–1202 https://doi.org/10.1038/nmat4719.
[41] F. Hang, A.H. Barber, Nano-mechanical properties of individual mineralized collagen fibrils from bone tissue, J. R. Soc. Interface. 8 (2011) 500–505 https://doi.org/10.1098/rsif.2010.0413.
[42] P.K. Zysset, Indentation of bone tissue: A short review, Osteoporos. Int. 20 (2009) 1049–1055 https://doi.org/10.1007/s00198-009-0854-9.
[43] X. Chen, N. Ogasawara, M. Zhao, N. Chiba, On the uniqueness of measuring elastoplastic properties from indentation: The indistinguishable mystical materials, J. Mech. Phys. Solids. 55 (2007) 1618–1660 https://doi.org/10.1016/j.jmps.2007.01.010.
[44] M.D. Uchic, D.M. Dimiduk, A methodology to investigate size scale effects in crystalline plasticity using uniaxial compression testing, Mater. Sci. Eng. A 400–401 (2005) 268–278 https://doi.org/10.1016/j.msea.2005.03.082.
[45] E.M. Spiesz, P.K. Zysset, Structure-mechanics relationships in mineralized tendons, J. Mech. Behav. Biomed. Mater. 52 (2015) 72–84 https://doi.org/10.1016/j.jmbbm.2015.03.013.
[46] I. Jäger, P. Fratzl, Mineralized collagen fibrils: A mechanical model with a staggered arrangement of mineral particles, Biophys. J 79 (2000) 1737–1746 https://doi.org/10.1016/S0006-3495(00)76426-5.
[47] E.M. Spiesz, P. Roschger, P.K. Zysset, Elastic anisotropy of uniaxial mineralized collagen fibers measured using two-directional indentation. Effects of hydration state and indentation depth, J. Mech. Behav. Biomed. Mater. 12 (2012) 20–28 https://doi.org/10.1016/j.jmbbm.2012.03.004.
[48] É. Budyn, J. Jonvaux, C. Funfschilling, T. Hoc, Bovine cortical bone stiffness and local strain are affected by mineralization and morphology, J. Appl. Mech. Trans. ASME. 79 (2012) 1–12 https://doi.org/10.1115/1.4004644.
[49] G. Poumarat, P. Squire, Comparison of mechanical properties of human, bovine bone and a new processed bone xenograft, Biomaterials 14 (1993) 337–340 https://doi.org/10.1016/0142-9612(93)90051-3.
[50] W. Wagermaier, H.S. Gupta, A. Gourrier, M. Burghammer, P. Roschger, P. Fratzl, Spiral twisting of fiber orientation inside bone lamellae, Biointerphases 1 (2006) 1–5 https://doi.org/10.1116/1.2178386.
[51] M. Müller, Introduction to Confocal and Fluorescence Microscopy, Second edi, SPIE, Bellingham, WA, 2006.
[52] G. Van Rossum, F.L. Drake, Python 3 Reference Manual, CreateSpace, Scotts Valley, CA, 2009.
[53] G.S. Mandair, M.D. Morris, Contributions of Raman spectroscopy to the understanding of bone strength, Bonekey Rep 4 (2015) 1–8 https://doi.org/10.1038/bonekey.2014.115.
[54] S. Gamsjaeger, R. Mendelsohn, A.L. Boskey, S. Gourion-Arsiquaud, K. Klaushofer, E.P. Paschalis, Vibrational spectroscopic imaging for the evaluation of matrix and mineral chemistry, Curr. Osteoporos. Rep 12 (2014) 454–464 https://doi.org/10.1007/s11914-014-0238-8.
[55] A. Masic, L. Bertinetti, R. Schuetz, L. Galvis, N. Timofeeva, J.W.C. Dunlop, J. Seto, M.A. Hartmann, P. Fratzl, Observations of multiscale, stress-induced changes of collagen orientation in tendon by polarized Raman spectroscopy, Biomacromolecules 12 (2011) 3989–3996 https://doi.org/10.1021/bm201008b.
[56] S.A. Overman, G.J. Thomas, Amide modes of the α-helix: Raman spectroscopy of filamentous virus fd containing peptide 13C and 2H labels in coat protein subunits, Biochemistry 37 (1998) 5654–5665 https://doi.org/10.1021/bi972339c.
[57] M. Janko, P. Davydovskaya, M. Bauer, A. Zink, R.W. Stark, Anisotropic Raman scattering in collagen bundles, Opt. Lett 35 (2010) 2765 https://doi.org/10.1364/ol.35.002765.
[58] M. Kazanci, P. Roschger, E.P. Paschalis, K. Klaushofer, P. Fratzl, Bone osteonal tissues by Raman spectral mapping : Orientation – composition, J. Struct. Biol. 156 (2006) 489–496 https://doi.org/10.1016/j.jsb.2006.06.011.
[59] H.Q. Bao, R.B. Li, H.D. Xing, C. Qu, Q. Li, W. Qiu, Crystalline orientation identification of phosphorene using polarized Raman spectroscopy without analyzer, Appl. Sci 9 (2019) https://doi.org/10.3390/app9112198.
[60] A. Roschger, S. Gamsjaeger, B. Hofstetter, A. Masic, S. Blouin, P. Messmer, A. Berzlanovich, E.P. Paschalis, P. Roschger, K. Klaushofer, P. Fratzl, Relationship between the v2PO4/amide III ratio assessed by Raman spectroscopy and the calcium content measured by quantitative backscattered electron microscopy in healthy human osteonal bone, J. Biomed. Opt. 19 (2014) 065002 https://doi.org/10.1117/1.jbo.19.6.065002.
[61] O. Akkus, F. Adar, M.B. Schaffler, Age-related changes in physicochemical properties of mineral crystals are related to impaired mechanical function of cortical bone, Bone 34 (2004) 443–453 https://doi.org/10.1016/j.bone.2003.11.003.
[62] M.D. Morris, G.S. Mandair, Raman Assessment of Bone Quality, Clin. Orthop. Relat. Res 469 (2011) 2160–2169 https://doi.org/10.1007/s11999-010-1692-y.
[63] Y.N. Yeni, J. Yerramshetty, O. Akkus, C. Pechey, C.M. Les, Effect of fixation and embedding on Raman spectroscopic analysis of bone tissue, Calcif. Tissue Int 78 (2006) 363–371 https://doi.org/10.1007/s00223-005-0301-7.
[64] M. Kazanci, H.D. Wagner, N.I. Manjubala, H.S. Gupta, E. Paschalis, P. Roschger, P. Fratzl, Raman imaging of two orthogonal planes within cortical bone, Bone 41 (2007) 456–461 https://doi.org/10.1016/j.bone.2007.04.200.
[65] O.L. Katsamenis, H.M.H. Chong, O.G. Andriotis, P.J. Thurner, Load-bearing in cortical bone microstructure: Selective stiffening and heterogeneous strain distribution at the lamellar level, J. Mech. Behav. Biomed. Mater. 17 (2013) 152–165 https://doi.org/10.1016/j.jmbbm.2012.08.016.
[66] S. Tadimalla, M.C. Tourell, R. Knott, K.I. Momot, Quantifying collagen fibre architecture in articular cartilage using small-angle X-ray scattering, Biomed. Spectrosc. Imaging 6 (2017) 37–57 https://doi.org/10.3233/bsi-170164.
[67] A.K. Maurya, L. Weidenbacher, F. Spano, G. Fortunato, R.M. Rossi, M. Frenz, A. Dommann, A. Neels, A. Sadeghpour, Structural insights into semicrystalline states of electrospun nanofibers: A multiscale analytical approach, Nanoscale 11 (2019) 7176–7187 https://doi.org/10.1039/c9nr00446g.
[68] W. Ruland, Small-angle scattering studies on carbonized cellulose fibers, J. Polym. Sci. Part C Polym. Symp. 28 (1969) 143–151 https://doi.org/10.1002/polc.5070280113.
[69] S. Ran, D. Fang, X. Zong, B.S. Hsiao, B. Chu, P.M. Cunniff, Structural changes during deformation of Kevlar fibers via on-line synchrotron SAXS/WAXD techniques, Polymer (Guildf) (2001) https://doi.org/10.1016/S0032-3861(00)00460-2.
[70] C.T. Rueden, J. Schindelin, M.C. Hiner, B.E. DeZonia, A.E. Walter, E.T. Arena, K.W. Eliceiri, ImageJ2: ImageJ for the next generation of scientific image data, BMC Bioinformatics 18 (2017) 1–26 https://doi.org/10.1186/s12859-017-1934-z.
[71] M. Doube, M.M. Kłosowski, I. Arganda-carreras, P. Fabrice, BoneJ : free and extensible bone image analysis in ImageJ, Bone 47 (2010) 1076–1079 https://doi.org/10.1016/j.bone.2010.08.023.BoneJ.
[72] H. Zhang, B.E. Schuster, Q. Wei, K.T. Ramesh, The design of accurate micro-compression experiments, Scr. Mater 54 (2006) 181–186 https://doi.org/10.1016/j.scriptamat.2005.06.043.
[73] S.W. Tsai, E.M. wu, A General Theory of Strength for Anisotropic Materials, J. Compos. Mater. 5 (1971) 58–80 https://doi.org/10.1177/002199837100500106.
[74] MATLAB, 9.7.0.1190202 (R2019b), The MathWorks Inc., Natick, Massachusetts, 2018.
[75] A.H. Burstein, J.M. Zika, K.G. Heiple, L. Klein, Contribution of collagen and mineral to the elastic-plastic properties of bone., J. Bone Joint Surg. Am. 57 (1975) 956–961 http://www.ncbi.nlm.nih.gov/pubmed/1184645.
[76] M. Raghavan, Investigation of Mineral and Collagen Organization in Bone Using Raman Spectroscopy, 2011.
[77] S. Mortazavian, A. Fatemi, Effects of fiber orientation and anisotropy on tensile strength and elastic modulus of short fiber reinforced polymer composites, Compos. Part B Eng 72 (2015) 116–129 https://doi.org/10.1016/j.compositesb.2014.11.041.
[78] E. Dall'Ara, D. Pahr, P. Varga, F. Kainberger, P. Zysset, QCT-based finite element models predict human vertebral strength in vitro significantly better than simulated DEXA, Osteoporos. Int 23 (2012) 563–572 https://doi.org/10.1007/s00198-011-1568-3.
[79] F. Johannesdottir, B. Allaire, M.L. Bouxsein, Fracture Prediction by Computed Tomography and Finite Element Analysis : Current and Future Perspectives, (2018) 411–422.
[80] E. Donnelly, Methods for assessing bone quality: A review, Clin. Orthop. Relat. Res 469 (2011) 2128–2138 https://doi.org/10.1007/s11999-010-1702-0.
[81] L. Mosekilde, Li. Mosekilde Department of Cell Biology, Institute of Anatomy, University of Aarhus DK-8000 Aarhus, Denmark, October. 17 (1995) 343S-352S. http://dx.doi.org/10.1016/8756-3282(95)00312-2.

[82] A.I. Pearce, R.G. Richards, S. Milz, E. Schneider, S.G. Pearce, Animal models for implant biomaterial research in bone: A review, Eur. Cells Mater 13 (2007) 1–10 https://doi.org/10.22203/eCM.v013a01.
[83] C.H. Turner, A. Chandran, R.M.V. Pidaparti, The anisotropy of osteonal bone and its ultrastructural implications, Bone 17 (1995) 85–89 https://doi.org/10.1016/8756-3282(95)00148-7.
[84] D. Carnelli, D. Gastaldi, V. Sassi, R. Contro, C. Ortiz, P. Vena, A finite element model for direction-dependent mechanical response to nanoindentation of cortical bone allowing for anisotropic post-yield behavior of the tissue, J. Biomech. Eng. 132 (2010) 1–10 https://doi.org/10.1115/1.4001358.
[85] S.F. Lipson, J.L. Katz, The relationship between elastic properties and microstructure of bovine cortical bone, J. Biomech. (1984) https://doi.org/10.1016/0021-9290(84)90134-9.
[86] G. Guidoni, M. Swain, I. Jäger, Nanoindentation of wet and dry compact bone: Influence of environment and indenter tip geometry on the indentation modulus, Philos. Mag 90 (2010) 553–565 https://doi.org/10.1080/14786430903201853.
[87] S. Li, E. Demirci, V.V. Silberschmidt, Variability and anisotropy of mechanical behavior of cortical bone in tension and compression, J. Mech. Behav. Biomed. Mater (2013) https://doi.org/10.1016/j.jmbbm.2013.02.021.
[88] Z. Manilay, E. Novitskaya, E. Sadovnikov, J. McKittrick, A comparative study of young and mature bovine cortical bone, Acta Biomater (2013) https://doi.org/10.1016/j.actbio.2012.08.040.
[89] C. Hellmich, A. Fritsch, L. Dormieux, Multiscale Homogenization Theory: An Analysis Tool for Revealing Mechanical Design Principles in Bone and Bone Replacement Materials, in: 2011: pp. 81–103. https://doi.org/10.1007/978-3-642-11934-7_5.
[90] D. Carnelli, P. Vena, M. Dao, C. Ortiz, R. Contro, Orientation and size-dependent mechanical modulation within individual secondary osteons in cortical bone tissue, J. R. Soc. Interface 10 (2013) https://doi.org/10.1098/rsif.2012.0953.
[91] J.Y. Rho, G.M. Pharr, Effects of drying on the mechanical properties of bovine femur measured by nanoindentation, J. Mater. Sci. Mater. Med. 10 (1999) 485–488 https://doi.org/10.1023/A:1008901109705.
[92] O.G. Andriotis, S. Desissaire, P.J. Thurner, Collagen Fibrils: Nature's Highly Tunable Nonlinear Springs, ACS Nano 12 (2018) 3671–3680 https://doi.org/10.1021/acsnano.8b00837.
[93] A.K. Bembey, A.J. Bushby, A. Boyde, V.L. Ferguson, M.L. Oyen, Hydration effects on the micro-mechanical properties of bone, J. Mater. Res. 21 (2006) 1962–1968 https://doi.org/10.1557/jmr.2006.0237.
[94] M. Maghsoudi-Ganjeh, X. Wang, X. Zeng, Computational investigation of the effect of water on the nanomechanical behavior of bone, J. Mech. Behav. Biomed. Mater (2020) https://doi.org/10.1016/j.jmbbm.2019.103454.
[95] L.M. Jenkins, A.M. Donald, Use of the environmental scanning electron microscope for the observation of the swelling behaviour of cellulosic fibres, Scanning 19 (1997) 92–97 https://doi.org/10.1002/sca.4950190206.
[96] A. Masic, L. Bertinetti, R. Schuetz, S.W. Chang, T.H. Metzger, M.J. Buehler, P. Fratzl, Osmotic pressure induced tensile forces in tendon collagen, Nat. Commun 6 (2015) 1–8 https://doi.org/10.1038/ncomms6942.
[97] H. Peterlik, P. Roschger, K. Klaushofer, P. Fratzl, From brittle to ductile fracture of bone, Nat. Mater 5 (2006) 52–55 https://doi.org/10.1038/nmat1545.
[98] H.S. Gupta, U. Stachewicz, W. Wagermaier, P. Roschger, H.D. Wagner, P. Fratzl, Mechanical modulation at the lamellar level in osteonal bone, J. Mater. Res. 21 (2006) 1913–1921 https://doi.org/10.1557/jmr.2006.0234.
[99] S. Morgan, A.A. Poundarik, D. Vashishth, Do Non-collagenous Proteins Affect Skeletal Mechanical Properties? Calcif. Tissue Int 97 (2015) 281–291 https://doi.org/10.1007/s00223-015-0016-3.
[100] H.S. Gupta, W. Wagermaier, G.A. Zickler, D.R. Ben Aroush, S.S. Funari, P. Roschger, H.D. Wagner, P. Fratzl, Nanoscale deformation mechanisms in bone, Nano Lett 5 (2005) 2108–2111 https://doi.org/10.1021/nl051584b.
[101] P.K. Hansma, G.E. Fantner, J.H. Kindt, P.J. Thurner, G. Schitter, P.J. Turner, S.F. Udwin, M.M. Finch, Sacrificial bonds in the interfibrillar matrix of bone, J. Musculoskelet. Neuronal Interact. 5 (2005) 313–315.
[102] A.G. Reisinger, D.H. Pahr, P.K. Zysset, Principal stiffness orientation and degree of anisotropy of human osteons based on nanoindentation in three distinct planes, J. Mech. Behav. Biomed. Mater. 4 (2011) 2113–2127 https://doi.org/10.1016/j.jmbbm.2011.07.010.
[103] J.G. Swadener, J.-Y. Rho, G.M. Pharr, Effects of anisotropy on elastic moduli measured by nanoindentation in human tibial cortical bone, J. Biomed. Mater. Res. 57 (2001) 108–112 https://doi.org/10.1002/1097-4636(200110)57:1⟨108::AID-JBM1148⟩3.0.CO;2-6.
[104] G. Franzoso, P.K. Zysset, Elastic anisotropy of human cortical bone secondary osteons measured by nanoindentation, J. Biomech. Eng. 131 (2009) 1–11 https://doi.org/10.1115/1.3005162.
[105] H.S. Gupta, J. Seto, W. Wagermaier, P. Zaslansky, P. Boesecke, P. Fratzl, Cooperative deformation of mineral and collagen in bone at the nanoscale, Proc. Natl. Acad. Sci. U. S. A. 103 (2006) 17741–17746 https://doi.org/10.1073/pnas.0604237103.
[106] S.E. Szczesny, D.M. Elliott, Incorporating plasticity of the interfibrillar matrix in shear lag models is necessary to replicate the multiscale mechanics of tendon fascicles, J. Mech. Behav. Biomed. Mater. 40 (2014) 325–338 https://doi.org/10.1016/j.jmbbm.2014.09.005.
[107] I. Jäger, P. Fratzl, Mineralized collagen fibrils: A mechanical model with a staggered arrangement of mineral particles, Biophys. J (2000) https://doi.org/10.1016/S0006-3495(00)76426-5.
[108] K. Tai, F.J. Ulm, C. Ortiz, Nanogranular origins of the strength of bone, Nano Lett 6 (2006) 2520–2525 https://doi.org/10.1021/nl061877k.
[109] D.M.L. Cooper, A.L. Turinsky, C.W. Sensen, B. Hallgrímsson, Quantitative 3D analysis of the canal network in cortical bone by micro-computed tomography, Anat. Rec. Part B New Anat 274B (2003) 169–179 https://doi.org/10.1002/ar.b.10024.
[110] D.M.L. Cooper, C.E. Kawalilak, K. Harrison, B.D. Johnston, J.D. Johnston, Cortical Bone Porosity: What Is It, Why Is It Important, and How Can We Detect It? Curr. Osteoporos. Rep. 14 (2016) 187–198 https://doi.org/10.1007/s11914-016-0319-y.
[111] Y.C. Lim, K.J. Altman, D.F. Farson, K.M. Flores, Micropillar fabrication on bovine cortical bone by direct-write femtosecond laser ablation, J. Biomed. Opt. 14 (2009) 064021 https://doi.org/10.1117/1.3268444.